Monthly Notices of the ROYAL ASTRONOMICAL SOCIETY

MNRAS **458,** 1199–1213 (2016)
Advance Access publication 2016 February 9

doi:10.1093/mnras/stw300

Hα kinematics of S^{4}G spiral galaxies – III. Inner rotation curves

Santiago Erroz-Ferrer,[1,2,3★] Johan H. Knapen,[1,2★] Ryan Leaman,[1,2,4] Simón Díaz-García,[5] Heikki Salo,[5] Eija Laurikainen,[5,6] Miguel Querejeta,[4] Juan Carlos Muñoz-Mateos,[7] E. Athanassoula,[8] Albert Bosma,[8] Sebastien Comerón,[5,6] Bruce G. Elmegreen[9] and Inma Martínez-Valpuesta[1,2]

[1]*Instituto de Astrofísica de Canarias, Vía Láctea s/n, E-38205 La Laguna, Spain*
[2]*Departamento de Astrofísica, Universidad de La Laguna, E-38206 La Laguna, Spain*
[3]*Department of Physics, Institute for Astronomy, ETH Zurich, CH-8093 Zurich, Switzerland*
[4]*Max-Planck-Institut für Astronomie/Königstuhl 17, D-69117 Heidelberg, Germany*
[5]*Department of Physical Sciences, Astronomy Division, FIN-90014 University of Oulu, PO Box 3000, Oulu, Finland*
[6]*Finnish Centre of Astronomy with ESO (FINCA), University of Turku, Väisäläntie 20, FI-21500 Piikkiö, Finland*
[7]*European Southern Observatory, Casilla 19001, Santiago 19, Chile*
[8]*Aix Marseille Université CNRS, LAM (Laboratoire d'Astrophysique de Marseille) UMR 7326, F-13388 Marseille, France*
[9]*IBM Research Division, T.J. Watson Research Center, Yorktown Hts., NY 10598, USA*

Accepted 2016 February 5. Received 2016 February 3; in original form 2015 June 25

ABSTRACT

We present a detailed study of the shape of the innermost part of the rotation curves of a sample of 29 nearby spiral galaxies, based on high angular and spectral resolution kinematic Hα Fabry–Perot observations. In particular, we quantify the steepness of the rotation curve by measuring its slope $d_R v_c(0)$. We explore the relationship between the inner slope and several galaxy parameters, such as stellar mass, maximum rotational velocity, central surface brightness (μ_0), bar strength and bulge-to-total ratio. Even with our limited dynamical range, we find a trend for low-mass galaxies to exhibit shallower rotation curve inner slopes than high-mass galaxies, whereas steep inner slopes are found exclusively in high-mass galaxies. This trend may arise from the relationship between the total stellar mass and the mass of the bulge, which are correlated among them. We find a correlation between the inner slope of the rotation curve and the morphological T-type, complementary to the scaling relation between $d_R v_c(0)$ and μ_0 previously reported in the literature. Although we find that the inner slope increases with the Fourier amplitude A_2 and decreases with the bar torque Q_b, this may arise from the presence of the bulge implicit in both A_2 and Q_b. As previously noted in the literature, the more compact the mass in the central parts of a galaxy (more concretely, the presence of a bulge), the steeper the inner slopes. We conclude that the baryonic matter dominates the dynamics in the central parts of our sample galaxies.

Key words: galaxies: kinematics and dynamics – galaxies: spiral.

1 INTRODUCTION

Rotation curves have been extensively used in the literature as tracers of the distribution of mass in spiral galaxies. The link between the shape of the rotation curve and the amount of luminous (baryonic) and dark matter (DM) provides important information about the formation and evolution of galaxies. One of the first pieces of evidence for the presence of DM in galaxies was the flat part of H I rotation curves (Bosma 1981; van Albada 1985; van Albada & Sancisi 1986; Begeman 1987), because such flat H I rotation curves extend to much larger radii than optical data, where DM is thought to dominate the gravitational potential (Rogstad & Shostak 1972; Roberts & Whitehurst 1975; Bosma 1978, 1981).

On the one hand, Burstein & Rubin (1985) and Rubin et al. (1985) defended that the shape of the rotation curve (and therefore the mass distribution) does not depend on morphological type, luminosity, total mass, bulge-to-disc ratio or other global properties of the galaxies, suggesting that the form of the gravitational potential is not correlated with the light distribution. Persic & Salucci (1991) and Persic, Salucci & Stel (1996) presented the idea of a universal rotation curve as a function of few parameters capable of representing any rotation curve of late-type spiral galaxies, such as the total luminosity of the galaxy together with the disc scale length. But on the other hand, other studies defend that the total luminosity of the galaxy and other galaxy properties (i.e.

★E-mail: serroz86@gmail.com (SE-F); jhk@iac.es (JHK)

presence of a bulge) influence the shape of the rotation curve (Corradi & Capaccioli 1990; Casertano & van Gorkom 1991; Broeils 1992; Verheijen 1997, 2001; Swaters 1999; Matthews & Gallagher 2002; Swaters et al. 2003 and Sancisi 2004, among others).

Several studies of H I rotation curves have analysed the shape of the rotation curve (e.g. de Blok, McGaugh & van der Hulst 1996; Swaters 1999; Côté, Carignan & Freeman 2000; Verheijen 2001; Gentile et al. 2004; Noordermeer et al. 2007; Swaters et al. 2009, 2011, 2012), including all types of morphologies, luminosities and galaxy properties (e.g. both high- and low-surface brightness galaxies). Few studies have performed a quantitative study of the shapes of rotation curves. In particular, Swaters et al. (2009) parametrized the shape of the rotation curve with the logarithmic slope $S = \Delta \log v / \Delta \log R$, looking for correlations between the logarithmic slope and the central surface brightness or morphological type. They concluded that for both spiral and late-type dwarf galaxies, the correlation between the light distribution and the inner rotation curve shape suggests that galaxies with higher central light concentration also have higher central mass densities, which implies that the luminous mass dominates over the DM mass in the gravitational potential in the central regions.

One of the most recent quantitative studies of the inner slopes of rotation curves was presented by Lelli et al. (2013, hereafter LFV13). They found a scaling relation between the circular velocity gradient $d_R V(0)$ (what we will refer to as the slope of the circular velocity curve) and the central surface brightness μ_0 over more than two orders of magnitude in $d_R V(0)$ and four orders of magnitudes in μ_0. This scaling relation for disc galaxies shows a clear relationship between the stellar density of a galaxy in the centre and the inner shape of the potential well, also for low-surface brightness galaxies where DM is thought to dominate in the central regions.

The inner shape of rotation curves derived from low-resolution H I data can be influenced by several systematic effects. For such data, tests have shown that there is a minimum number of independent points necessary to get a reasonable description of a rotation curve (see chapter 3.4 of Bosma 1978[1]). For highly inclined galaxies, radial velocities based on moment equations are skewing the data to velocities closer to the systemic velocity (e.g. Sancisi, Allen & Sullivan 1979), and the envelope tracing method advocated by Sofue (1996, 1997) might be more appropriate. One possible solution is supplementing the H I data with higher resolution data in the inner parts using either Hα or CO studies (e.g. van der Kruit & Bosma 1978; Corradi et al. 1991; Sofue 1997; Blais-Ouellette et al. 2004; Noordermeer et al. 2005; LFV13). Also, several techniques have been developed to take beam-smearing effects in account: position-velocity diagrams along the major axis (e.g. Begeman 1987; Broeils 1992; Verheijen & Sancisi 2001) or 3D model cubes that consider many observational effects such as the spatial and spectral resolution, velocity dispersion or gas distribution (e.g. Gentile et al. 2004; Swaters et al. 2009; Lelli, Fraternali & Sancisi 2010; Lelli et al. 2012a,b; Lelli, Verheijen & Fraternali 2014b).

In order to obtain the highest possible angular resolution for our sample of nearby galaxies, we used Hα Fabry-Perot (FP) data from the observational survey introduced in Erroz-Ferrer et al. (2012, hereafter Paper I) and described in detail in Erroz-Ferrer et al. (2015, hereafter Paper II). These data have high angular (seeing limited, $\sim$1 arcsec) and spectral ($\sim$8 km s^{-1} sampling) resolutions, higher than data from other FP studies such as those from the Virgo survey (Chemin et al. 2006) or the GHASP survey (see Epinat, Amram & Marcelin 2008, for a complete description of the GHASP sample and data), or typical H I data (e.g. THINGS is one of the H I surveys with the highest angular resolution, of $\sim$6 arcsec; Walter et al. 2008).

This paper is organized as follows: Section 2 gives a description of the sample selection, the observations and the data reduction and data analysis. The derived results are presented in Section 3 and discussed in Section 4. Section 5 presents our conclusions.

2 THE DATA

2.1 Sample, observations and data reduction

The sample is described in Paper II and consists of 29 galaxies spread in morphological type and other characteristics such as bar presence. Information about the galaxies can be found in Table 1. All these galaxies are part of the *Spitzer* Survey of Stellar Structure in Galaxies (S^{4}G; Sheth et al. 2010). The S^{4}G survey has delivered 3.6 and 4.5 μm images of more than 2350 galaxies to the scientific community.[2] All the mid-infrared (IR) images have been processed using the S^{4}G pipelines, and we use some of the products from these for our 29 galaxies (presented in Table 1): (i) surface brightness profiles, from Muñoz-Mateos et al. (2015); (ii) bulge-to-total ratios (B/T) derived from the 2D structural decompositions presented in Salo et al. (2015) and (iii) the stellar mass maps (Querejeta et al. 2015). In addition, we use the mid-IR morphological classifications and T-types from Buta et al. (2015); and bar torques (Q_b) and bar lengths from Díaz-García et al. (2015) and Herrera-Endoqui et al. (2015).

The kinematic data have been obtained with the GHαFaS (Galaxy Hα Fabry–Perot System) instrument mounted on the William Herschel Telescope (WHT) in La Palma. In this study, we use the first and second moment maps derived from the GHαFaS kinematic cubes (the velocity and velocity dispersion maps). The high angular resolution of GHαFaS allows us to derive high-resolution rotation curves ($\sim$1 arcsec sampling). We use the ROTCUR task in GIPSY, based on the tilted-ring method explained in Begeman (1989). The velocity maps and derived rotation curves have been presented in Paper II, along with all the details about the observations and data reduction processes.

The FP data were observed along with Hα narrow-band images using the Auxiliary port CAMera (ACAM), also at the WHT. The Hα narrow-band images have two aims. First, the kinematic cubes need to be flux calibrated, and the narrow-band images allow us to flux calibrate the intensity maps from the GHαFaS cubes as explained in Paper I and Paper II. Secondly, we can compute star formation rates (SFRs) derived from the measured fluxes in these narrow-band images.

2.2 Rotation curves derived from the stellar mass maps

To understand the stellar mass distribution, we have estimated the circular velocity from the observed photometric data, in particular, the stellar mass maps from Querejeta et al. (2015), using the mass-to-light ratio (M/L = 0.6) from Meidt et al. (2014). The stellar mass maps are the result of applying the Independent Component Analysis method first introduced by Meidt et al. (2012) to the 3.6 and 4.5 μm images of the galaxies. This method separates the light from old stars by removing the contribution due to polycyclic aromatic hydrocarbon, hot dust and intermediate-age stars. As shown by

[1] http://ned.ipac.caltech.edu/level5/March05/Bosma/frames.html

[2] http://irsa.ipac.caltech.edu/data/SPITZER/S4G/

Table 1. General properties of the galaxies in the sample. Notes: (1) Mean *T*-types from the two independent morphological classifications in Buta et al. (2015). (2) Central surface brightness obtained following the procedure by LFV13 and measured from the light profiles derived with ellipse fitting to the 3.6 μm images (Muñoz-Mateos et al. 2015). (3) Bar strengths derived from the torque maps obtained from the 3.6 μm images (Díaz-García et al. 2015). (4) Bar lengths from Díaz-García et al. (2015) and Herrera-Endoqui et al. (2015). (5) *B/T* ratios from the structural 2D decompositions to the 3.6 μm images (Salo et al. 2015). (6) Total stellar masses (M_*) derived using the absolute magnitudes at 3.6 and 4.5 μm (from the ellipse fitting, Muñoz-Mateos et al. 2015), and derived using the recipes of Querejeta et al. (2015). The uncertainties in M_* include those arising from the uncertainty of 0.2 dex on M/L and the uncertainties in the absolute magnitudes.

Galaxy name	⟨T⟩	μ_0 (mag arcsec^{-2})	Q_b	Bar length (kpc)	*B/T*	$\log(M_*/M_\odot)$
	(1)	(2)	(3)	(4)	(5)	(6)
NGC 428	8.0	20.4 ± 0.2	0.29 ± 0.03	2.41	0.002	9.72 ± 0.13
NGC 691	2.0	17.6 ± 0.7	0.00 ± 0.00	0.00	0.170	10.70 ± 0.13
NGC 864	4.0	18.0 ± 0.5	0.47 ± 0.07	3.85	0.027	10.17 ± 0.13
NGC 918	6.0	19.6 ± 0.4	0.23 ± 0.02	0.85	0.008	10.09 ± 0.13
NGC 1073	5.5	19.4 ± 0.6	0.63 ± 0.08	4.14	0.000	9.95 ± 0.13
NGC 2500	6.5	20.4 ± 0.3	0.28 ± 0.03	1.56	0.002	9.39 ± 0.13
NGC 2541	7.5	21.0 ± 0.4	0.00 ± 0.00	0.00	0.000	9.41 ± 0.13
NGC 2543	3.0	16.1 ± 0.8	0.35 ± 0.08	5.67	0.165	10.40 ± 0.13
NGC 2712	2.5	16.0 ± 0.8	0.28 ± 0.05	4.00	0.170	10.41 ± 0.13
NGC 2748	4.0	18.2 ± 0.5	0.45 ± 0.03	1.66	0.034	10.30 ± 0.13
NGC 2805	5.0	19.7 ± 0.6	0.19 ± 0.01	2.13	0.002	10.32 ± 0.13
NGC 3041	3.5	18.7 ± 0.3	0.00 ± 0.00	0.00	0.043	10.40 ± 0.13
NGC 3403	5.0	19.4 ± 0.6	0.00 ± 0.00	0.00	0.000	10.10 ± 0.13
NGC 3423	4.5	19.1 ± 0.5	0.00 ± 0.00	0.00	0.055	9.69 ± 0.13
NGC 3504	1.0	14.5 ± 1.4	0.25 ± 0.06	4.59	0.364	10.43 ± 0.13
NGC 4151	0.0	15.8 ± 1.1	0.09 ± 0.02	6.38	0.443	9.91 ± 0.13
NGC 4324	− 1.0	15.8 ± 0.9	0.00 ± 0.00	0.00	0.326	10.66 ± 0.13
NGC 4389	1.0	18.3 ± 0.4	0.52 ± 0.06	2.81	0.000	9.82 ± 0.13
NGC 4498	7.0	19.6 ± 0.4	0.46 ± 0.07	2.26	0.000	9.72 ± 0.13
NGC 4639	2.0	16.4 ± 0.7	0.26 ± 0.04	2.09	0.112	10.28 ± 0.13
NGC 5112	6.5	20.1 ± 0.4	0.62 ± 0.06	1.66	0.000	10.11 ± 0.13
NGC 5334	6.0	20.4 ± 0.3	0.49 ± 0.08	2.36	0.001	10.38 ± 0.13
NGC 5678	3.0	17.5 ± 0.4	0.00 ± 0.00	0.00	0.037	10.74 ± 0.13
NGC 5740	2.0	16.0 ± 0.7	0.16 ± 0.03	3.05	0.125	10.43 ± 0.13
NGC 5921	3.0	16.2 ± 1.0	0.34 ± 0.06	6.57	0.111	10.39 ± 0.13
NGC 6070	5.0	17.9 ± 0.5	0.00 ± 0.00	0.00	0.045	10.71 ± 0.13
NGC 6207	6.5	19.2 ± 0.2	0.21 ± 0.02	2.75	0.000	10.06 ± 0.13
NGC 6412	6.0	18.8 ± 0.5	0.24 ± 0.02	1.08	0.005	10.11 ± 0.13
NGC 7241	5.5	18.5 ± 0.4	0.00 ± 0.00	0.00	0.000	10.28 ± 0.13

Meidt et al. (2014) and confirmed by Norris et al. (2014) and Röck et al. (2015), the 3.6 μm band has the advantage that, once dust has been corrected for, a uniform $M/L = 0.6$ converts the stellar flux into stellar mass, with an uncertainty smaller than 0.1 dex. The difference between the raw 3.6 μm images and the stellar mass maps is typically between 10 and 40 per cent, but can be practically negligible (e.g. for NGC 691, NGC 2500 or NGC 4324). The location of the non-stellar emission also varies within the galaxy (see Querejeta et al. 2015 for a full explanation of the stellar mass maps computation).

The radial force map obtained to compute the bar strength using the NIRQB code (Laurikainen & Salo 2002 and Salo et al. 2010) based on the polar method (Salo et al. 1999) is used to compute the stellar component of the circular velocity[3] as

$$v_*^2 = r\frac{\partial \Phi_*}{\partial r} = rF_r, \quad (1)$$

where F_r is the radial force obtained as the partial derivative of the potential Φ_*. The gravitational potential is calculated using the polar method: from the deprojected *Spitzer* images, the even Fourier components $I(r, \varphi)$ are calculated within a polar grid. Then, the gravitational potential is calculated by adding the fast Fourier transformation in the azimuthal direction in combination with a direct summation of the radial and vertical directions. Three different disc scaleheights (h_z) have been used to compute the potential: $h_z = 0.05$ R_{K20}, $h_z = 0.1$ R_{K20} and $h_z = 0.2$ R_{K20}, where R_{K20} is the 2MASS 20 mag arcsec^{-2} isophote. The value of $h_z = 0.1$ R_{K20} is statistically the closest to reality, based on the observations of edge-on galaxies carried out by de Grijs & Peletier (1997) and the study of Speltincx, Laurikainen & Salo (2008). The other two disc thickness values provide a margin of uncertainty in our method.

This method yields a numerical solution to the Poisson equation consistent with the method described in Casertano (1983). For test purposes, Laurikainen & Salo (2002) also applied the Cartesian potential evaluation (e.g. Quillen, Frogel & Gonzalez 1994) using a two-dimensional Fast Fourier Transformation as in Buta & Block (2001), showing that the polar method behaves better than measuring noisy and weak structures due to the Fourier smoothing. We have not included in a detailed way the uncertainties arising from assuming a certain value of M/L. Assuming a typical uncertainty of 0.2 dex on M/L (see Querejeta et al. 2015), we can estimate typical uncertainties of 30 per cent in M_*, 15 per cent in v_* and 15 per cent

[3] We will refer to the stellar component of the circular velocity as v_*, leaving the notation v_c to the circular velocity derived from the Hα FP kinematic data, after inclination and ADCs are applied.

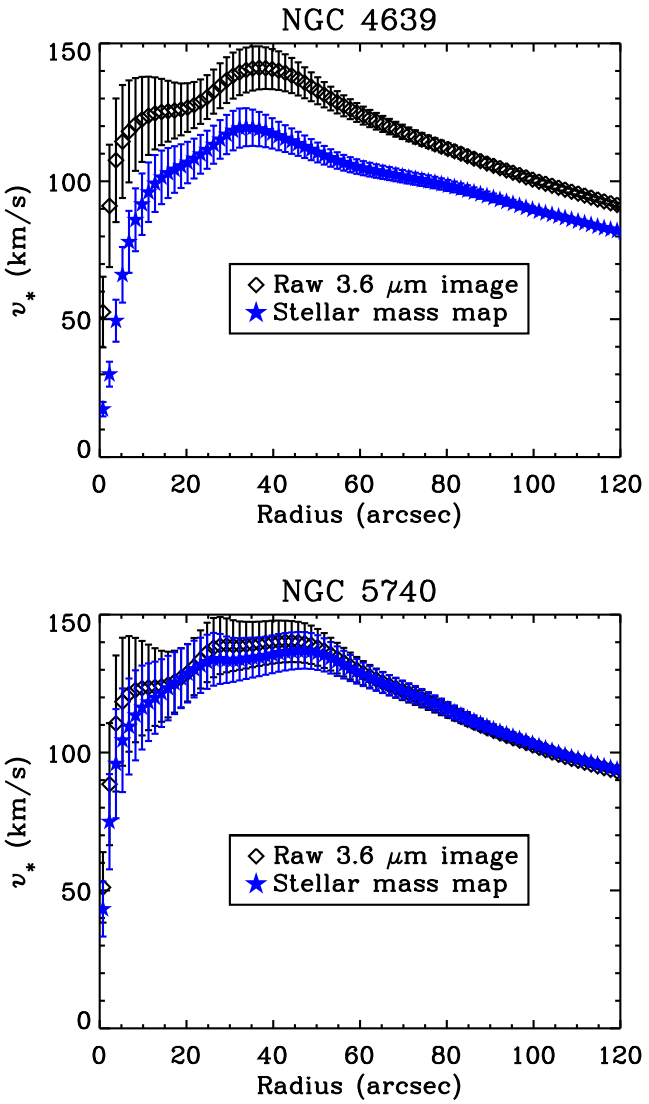

Figure 1. Circular velocity curves derived from the uncorrected 3.6 μm image (diamonds), and from the stellar mass map (blue stars) for NGC 4639 (top) and NGC 5740 (bottom), assuming a scaleheight of $h_z = 0.1\ R_{K20}$ and the same M/L from Meidt et al. (2014). The uncertainties indicate the difference between assuming a scaleheight of $h_z = 0.05\ R_{K20}$ and $h_z = 0.2\ R_{K20}$. We have not included the uncertainties arising from assuming a certain value of M/L. Assuming a typical uncertainty of 0.2 dex on M/L (see Querejeta et al. 2015), we can estimate typical uncertainties of 15 per cent in v_* and 15 per cent in the inner slope. The non-stellar emission in the raw 3.6 μm image leads to a significant overestimation of the derived circular velocity for NGC 4639. For NGC 5740, the non-stellar emission in the raw 3.6 μm image is not as important as in NGC 4639, but also leads to an overestimation of the derived circular velocity. The quantity and location of the non-stellar emission vary for each galaxy.

in the inner slope. As typical uncertainties on the inner slope from other sources amount to some 20 per cent, the additional uncertainty due to M/L cannot invalidate any of our results. A more detailed analysis of the effects of uncertainty in M/L is presented in Díaz-García et al. (2015).

We present in Fig. 1 the circular velocity curves derived from the uncorrected 3.6 μm images and from the stellar mass maps (hereafter stellar mass-derived rotation curves) for NGC 4639 and NGC 5740. We see that the difference between using the stellar mass maps and using the 3.6 μm images is very important for NGC 4639, but not that much for NGC 5740. In any case, the non-stellar emission present in the 3.6 μm images is translated into an overestimate of v_*, and the inner slope or the maximum rotational velocity is directly affected. Therefore, importantly, for this study we use the circular velocity curves (v_*) derived from the stellar mass maps. In Díaz-García et al. (2015), we test how much v_*, gravitational torques and Fourier decompositions change when using raw 3.6 μm data or stellar mass maps from Querejeta et al. (2015).

2.3 Asymmetric drift correction

Due to gravitational interactions between gas clouds, the observed Hα rotation velocities can be significantly lower than the circular velocities of a test particle under the same gravitational potential. Thus, we need to correct our observed Hα rotation curves for pressure support using the asymmetric drift correction (ADC; see e.g. section 4.8.2 of Binney & Tremaine 2008). The same gravitational interactions also show up in the velocity dispersion, and whenever this dispersion is significant, the ADC is not negligible. In these cases, we need to measure the velocity dispersion and compute the true circular velocity accounting for the ADC.

The circular velocity can be expressed as $v_c^2 = R(\partial\Phi/\partial R)$, and following equations 4–227 of Binney & Tremaine (2008):

$$v_c^2 = v_\phi^2 + \overline{v_\phi^2} - \overline{v_R^2} - \frac{R}{\nu}\frac{\partial(\nu\overline{v_R^2})}{\partial R} - R\frac{\partial(\overline{v_R v_z})}{\partial z}, \quad (2)$$

where ν is the 3D density and v_ϕ, v_R and v_z are the azimuthal, radial and vertical components of the velocity. We set $\overline{v_\phi^2} = \sigma_\phi^2$, $\overline{v_R^2} = \sigma_R^2$. We assume that the scaleheight of the disc is constant with radius, and therefore $\partial\ln\nu/\partial\ln R = \partial\ln\Sigma/\partial\ln R$, where Σ is the surface density profile (traced by the surface brightness profile). The Hα surface brightness profiles derived from the ACAM images (presented in the Appendix A) are fit to an exponential function $I = I_0 e^{-R/R_{\rm exp}}$, and the resulting $R_{\rm exp}$ are collected in Table 2. The peaks in the surface brightness profiles come from the emission of the H II regions. We assume that the velocity dispersion is isotropic, a reasonable hypothesis with gaseous discs. Thus, $\sigma_R = \sigma_z = \sigma_\phi = \sigma_{\rm obs}$.

Unlike the stellar velocity dispersion, the observed velocity dispersion in the ionized gas results from different phenomena: gravitational interaction between particles, thermal broadening, turbulent motions, natural broadening of the line ($\sigma_{\rm N}$) and instrumental width ($\sigma_{\rm inst}$). The only phenomena that reduces the observed velocity is the gravitational interaction, so we need to identify the other contributions and subtract them from the observed velocity dispersion. We assume that the turbulent and thermal components are physical drivers of the gravitational velocity dispersion ($\sigma_{\rm grav}$), and consider $\sigma_{\rm grav}$ the result of both thermal and turbulent motions in hydrodynamical equilibrium with the gravitational potential (e.g. Westfall et al. 2011). The instrumental width for each galaxy was obtained from a data cube taken with a calibration lamp, following the procedures in Relaño et al. (2005), and is 8.3 km s^{-1}. Here, we also need to subtract the natural broadening of the line ($\sigma_{\rm N} \approx 3$ km s^{-1}; O'dell & Townsley 1988). We obtain

$$\sigma_{\rm obs}^2 = \sigma_{\rm grav}^2 + \sigma_{\rm N}^2 + \sigma_{\rm inst}^2. \quad (3)$$

Table 2. Results from the photometric analysis on the light profiles (Hα and 3.6 μm surface brightness profiles) and exponential fits to the Hα velocity dispersion profiles. Column (1) Galaxy name. Column (2) Exponential radius $R_{\rm exp}$ of the Hα surface brightness profile. Column (3) Exponential radius $R_{{\rm exp},\sigma}$ derived from the velocity dispersion profiles. Column (4) Mean $\sigma_{\rm grav}$ for those galaxies without an exponential velocity dispersion profile.

Galaxy name	$R_{\rm exp}$ (kpc)	$R_{{\rm exp},\sigma}$ (kpc)	$\overline{\sigma}_{\rm grav}$ (km s^{-1})
NGC 428	2.97 ± 0.25	–	5.03 ± 0.45
NGC 691	9.19 ± 0.54	–	3.15 ± 0.34
NGC 864	2.85 ± 0.18	2.20 ± 0.34	–
NGC 918	3.60 ± 0.09	–	4.69 ± 0.36
NGC 1073	5.30 ± 0.54	–	5.06 ± 0.23
NGC 2500	2.60 ± 0.37	–	4.25 ± 0.24
NGC 2541	3.45 ± 0.32	–	6.12 ± 0.33
NGC 2543	3.38 ± 0.12	2.16 ± 0.40	–
NGC 2712	3.08 ± 0.07	3.29 ± 0.38	–
NGC 2748	1.43 ± 0.05	3.06 ± 0.58	–
NGC 2805	15.49 ± 0.60	–	6.02 ± 0.33
NGC 3041	4.13 ± 0.45	–	3.40 ± 0.18
NGC 3403	2.99 ± 0.10	–	3.68 ± 0.20
NGC 3423	1.65 ± 0.10	–	5.53 ± 0.32
NGC 3504	3.27 ± 0.10	3.75 ± 0.60	–
NGC 4151	5.96 ± 0.12	–	4.62 ± 0.35
NGC 4324	4.05 ± 0.19	–	3.39 ± 0.21
NGC 4389	2.20 ± 0.41	3.33 ± 0.78	–
NGC 4498	0.87 ± 0.04	2.08 ± 0.85	–
NGC 4639	1.72 ± 0.07	–	3.98 ± 0.26
NGC 5112	3.16 ± 0.15	–	4.68 ± 0.23
NGC 5334	3.51 ± 0.09	–	3.30 ± 0.41
NGC 5678	3.33 ± 0.10	–	5.53 ± 0.30
NGC 5740	1.83 ± 0.10	–	3.71 ± 0.34
NGC 5921	5.51 ± 0.33	–	3.42 ± 0.22
NGC 6070	2.99 ± 0.15	–	6.22 ± 0.44
NGC 6207	1.82 ± 0.05	–	6.12 ± 0.34
NGC 6412	1.97 ± 0.26	2.33 ± 0.54	–
NGC 7241	2.45 ± 0.07	–	5.27 ± 0.44

If we assume a Sérsic profile (Sérsic 1963), the ADC-corrected circular velocity can be expressed using equation A.6 of Lelli, Fraternali & Verheijen (2014a, hereafter LFV14):

$$v_{\rm c}^2 = v_{\rm rot}^2 + \sigma_{\rm grav}^2 \left[\frac{b_n}{n} \left(\frac{R}{R_{\rm eff}} \right)^{1/n} - 2 \frac{\partial \ln \sigma_{\rm grav}}{\partial \ln R} \right], \quad (4)$$

where n is the Sérsic index, b_n a constant dependant on n (see Ciotti 1991 and Ciotti & Bertin 1999) and $R_{\rm eff}$ the effective radius. For an exponential profile, $n = 1$, $b_1 = 1.678$ and $R_{\rm eff} = 1.678 \times R_{exp}$.

We have derived azimuthally averaged velocity dispersion profiles from the second moment maps of the galaxies (Paper II), and presented them in the Appendix B. For NGC 864, NGC 2543, NGC 2712, NGC 2748, NGC 3504, NGC 4389, NGC 4498 and NGC 6412, it is reasonable to assume an exponential function to $\sigma_{\rm grav}$, and then equation (4) simplifies to $v_{\rm c}^2 = v_{\rm rot}^2 + \sigma_{\rm grav}^2 (R/R_{\rm exp} + 2R/R_{{\rm exp},\sigma})$, where $R_{{\rm exp},\sigma}$ is the exponential scalelength of the velocity dispersion profiles. For the remaining galaxies, we assume a constant value of the dispersion $\overline{\sigma}_{\rm grav}$, although it does not fully represent the data as in most of the cases, the velocity dispersion profiles are dominated by the peaks from the H II regions. For these galaxies, equation (4) simplifies to $v_{\rm c}^2 = v_{\rm rot}^2 + \overline{\sigma}_{\rm grav}^2 (R/R_{\rm exp})$. These values of $R_{{\rm exp},\sigma}$ and $\overline{\sigma}_{\rm grav}$ are collected in Table 2.

The resulting circular velocity curves are therefore corrected for the slowdown caused by the gravitational interactions. We have implemented the ADC on our rotation curves and thus obtained the circular velocity curves. By definition, this correction is more significant in galaxies with higher σ. Also, in equation (4) we see that the higher the scalelength ($R_{\rm exp}$), the lower the correction. Therefore, the ADC is negligible in the central regions of most of the galaxies of our sample, like NGC 3041, where the resulting $v_{\rm c}$ curve is very similar to the observed rotation curve (Fig. 2). In Appendix C, we present the rotation curves and the ADC-corrected (circular) velocity curves for all the galaxies of our sample.

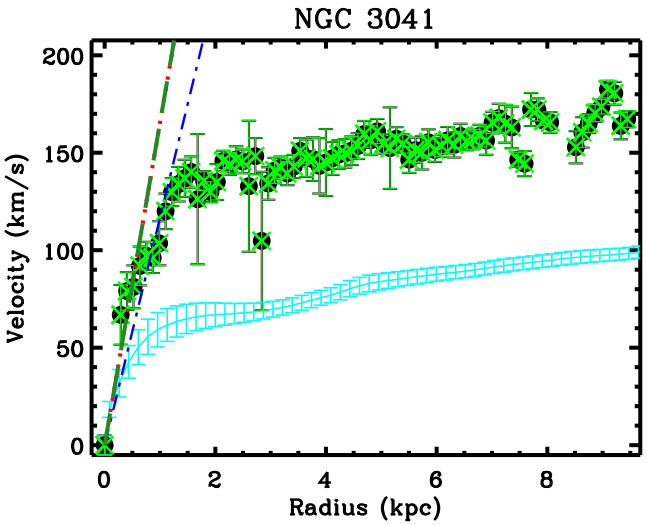

Figure 2. High resolution (1 arcsec) rotation curves for NGC 3041 derived from the FP data (circles), from the stellar mass maps (solid blue curve with errormarks) and after the ADC (circular velocity, green crosses). The inner slope of the curve has been highlighted with a red dotted line for the FP data, with a blue dot–dashed–dot line for the stellar mass rotation curve and with a green dashed line for the circular velocity curve. The polynomial is fitted to the points with radius below R_{90} (the radius where the curve reaches 90 per cent of the maximum velocity). The ADC is not important in this galaxy, and the circular velocity curve is very similar to the observed rotation curve. Most cases are like this one.

2.4 Determination of the rotation curve inner slopes

The motivation of this paper is to study the inner part of the rotation curve. To characterize this, we proceed as LFV13 by measuring the inner slope of the curve, hereafter $d_R V(0)$. The method consists of fitting a polynomial function with the form $V(R) = \sum_{n=1}^{m} a_n \times R^n$ to the inner part of the circular velocity curve (up to the radius where the curve reaches 90 per cent of the maximum velocity, R_{90}). The slope of the inner part is the term of the first order $a_1 = d_R V(0) = \lim_{R \to 0} {\rm d}V/{\rm d}R$, where the fit is forced to pass through $R = 0$ and $V = 0$. We refer the reader to LFV13 for more details about the method.

We have measured the inner slope of the observed Hα rotation curves $d_R v_{\rm rot}(0)$, of the ADC-corrected circular rotation curves for the FP data $d_R v_{\rm c}(0)$ and of the stellar mass-derived rotation curves $d_R v_*(0)$, and presented the results in Table 3. In Fig 2, we show the resulting fits to the observed, circular and mass rotation curves for our example galaxy NGC 3041, and the corresponding determination of the inner slopes, represented as the tangent line to the rotation curve at $R = 0$. Again, the rotation curves and fits for all the galaxies of the sample are presented in the Appendix C.

We have measured the inner slope of the circular velocity curve from our FP data in all the galaxies of the sample. The central regions of the galaxies NGC 4151, NGC 4324, NGC 4639, NGC 5740 and NGC 5921 are not sampled. These galaxies are mostly

Table 3. Results from the polynomial fits to the different rotation curves. Column (I): Galaxy name. Columns (II–IV) Inner slopes of the observed Hα rotation curves $d_R v_{\rm rot}(0)$, of the ADC-corrected circular rotation curves ($d_R v_{\rm c}(0)$) and of the stellar mass-derived rotation curves ($d_R v_*(0)$) correspondingly. Columns (V–VII) Radius where the curve reaches 90 per cent of the maximum velocity (R_{90}) for the observed Hα rotation curves ($R_{90,\rm rot}$), for the ADC-corrected circular rotation curves ($R_{90,\rm c}$) and for the stellar mass-derived rotation curves ($R_{90,*}$) correspondingly. Columns (VIII–X): order of the polynomial fit (m) to the observed Hα rotation curves ($m_{\rm rot}$), the ADC-corrected circular rotation curves ($m_{\rm c}$) and for the stellar mass-derived rotation curves (m_*) correspondingly.

Galaxy name	$d_R v_{\rm rot}(0)$ (km s^{-1} kpc^{-1})	$d_R v_{\rm c}(0)$ (km s^{-1} kpc^{-1})	$d_R v_*(0)$ (km s^{-1} kpc^{-1})	$R_{90,\rm rot}$ (kpc)	$R_{90,\rm c}$ (kpc)	$R_{90,*}$ (kpc)	$m_{\rm rot}$	$m_{\rm c}$	m_*
NGC 428	65 ± 22	65 ± 22	64 ± 2	5.74	5.74	2.83	4	4	3
NGC 691	139 ± 40	139 ± 40	236 ± 18	3.89	3.89	3.76	2	2	4
NGC 864	117 ± 34	122 ± 39	60 ± 2	2.48	2.48	6.16	2	1	4
NGC 918	108 ± 23	108 ± 23	55 ± 3	5.02	5.02	5.44	3	3	4
NGC 1073	164 ± 40	175 ± 42	73 ± 2	6.83	6.83	6.97	5	5	5
NGC 2500	105 ± 22	82 ± 17	98 ± 4	2.92	2.92	2.88	2	2	4
NGC 2541	48 ± 13	67 ± 14	57 ± 1	3.06	3.06	3.83	3	3	4
NGC 2543	412 ± 89	414 ± 89	139 ± 6	5.89	5.89	5.85	5	5	4
NGC 2712	410 ± 88	411 ± 89	156 ± 6	1.07	1.07	4.83	2	2	4
NGC 2748	212 ± 43	217 ± 44	232 ± 16	5.05	4.93	2.65	4	4	4
NGC 2805	22 ± 5	22 ± 5	54 ± 2	18.85	18.85	7.83	4	4	4
NGC 3041	165 ± 36	165 ± 36	117 ± 4	7.01	7.01	7.21	4	4	5
NGC 3403	211 ± 47	211 ± 47	117 ± 7	4.81	4.81	2.40	5	5	3
NGC 3423	122 ± 35	122 ± 35	102 ± 3	5.23	5.23	4.42	3	3	5
NGC 3504	639 ± 163	639 ± 163	720 ± 136	0.61	0.61	0.51	2	2	1
NGC 4151	650 ± 245	650 ± 245	440 ± 66	4.90	4.90	0.51	1	1	1
NGC 4324	133 ± 27	133[a] ± 27	944 ± 65	1.29	1.29	1.34	1	1	4
NGC 4389	80 ± 30	83 ± 30	83 ± 3	4.18	4.18	2.56	5	5	3
NGC 4498	46 ± 10	47 ± 10	102 ± 5	3.38	3.38	2.20	2	2	3
NGC 4639	210 ± 46	210[a] ± 46	275 ± 23	1.04	1.04	1.47	1	1	4
NGC 5112	39 ± 15	41 ± 15	50 ± 2	6.22	6.22	7.27	5	5	4
NGC 5334	38 ± 8	38 ± 8	37 ± 1	8.15	8.15	7.30	2	2	3
NGC 5678	243 ± 50	243[a] ± 50	258 ± 19	1.21	1.21	3.03	1	1	4
NGC 5740	97 ± 20	97[a] ± 21	422 ± 30	3.34	3.34	2.06	1	1	4
NGC 5921	42 ± 9	42[a] ± 9	224 ± 10	5.40	5.40	4.10	1	1	4
NGC 6070	105 ± 27	132 ± 33	80 ± 5	7.74	7.74	5.99	4	4	3
NGC 6207	75 ± 17	76 ± 17	152 ± 16	5.25	5.25	1.28	4	4	3
NGC 6412	111 ± 35	127 ± 40	58 ± 4	3.27	3.27	4.22	3	3	4
NGC 7241	32 ± 7	33 ± 7	102 ± 6	4.07	4.07	2.85	1	1	3

Note. [a]Lower limits of $d_R v_{\rm c}(0)$ for galaxies whose central parts were not fully sampled.

early-type barred galaxies. We have analysed those data equally as in the other galaxies in the sample in order to obtain lower limit values of $d_R v_{\rm rot}(0)$ and $d_R v_{\rm c}(0)$, which are highlighted in the forthcoming correlations with red arrows. For completeness, we have computed for these lower limits the observed inner slopes that LFV13 predict[4] from the μ_0, and these values are represented with red crosses in the forthcoming plots. The differences between the observed inner slopes and those predicted by Lelli's equation can be up to 30 per cent of $\log(d_R V(0))$, which is translated into a factor of 2 in the inner slope. This factor is exactly what LFV13 report as a realistic uncertainty for galaxies with compact inner components (bars or bulges) and poorly resolved rotation curves. NGC 4151 is a Seyfert 1.0 (Ho, Filippenko & Sargent 1997), and the central surface brightness may yield an overestimate of $d_R V(0)$. We therefore include the measurements from Fricke & Reinhardt (1974) which cover the central region, and measure an inner slope of $d_R V(0) = 650$ km s^{-1} kpc^{-1}, very similar to what would correspond to its morphological type (613 km s^{-1} kpc^{-1}, see Section 3.2). The H I rotation curve of NGC 4151 in Bosma, Ekers & Lequeux (1977) and Bosma (1981) cannot provide further information on the central parts, as beyond their first measured point at 1 arcmin, the velocity curve is flat with $v \sim 150$ km s^{-1}.

[4] The empirical relation in LFV13 is based on R-band photometry, and we therefore calculate the corresponding relationship for the 3.6 μm by using the correspondence between the surface brightness profiles for the Spitzer Infrared Nearby Galaxies Survey (SINGS) galaxies in the R band (Muñoz-Mateos et al. 2009) and 3.6 μm (Muñoz-Mateos et al. 2015): $\mu_R - \mu_{3.6} = 0.128\mu_{3.6} + 2.802$.

3 RESULTS: ROTATION CURVE INNER SLOPES AND PHYSICAL PROPERTIES OF GALAXIES

3.1 Comparison of inner slopes

We first present the relationships between the inner slopes measured using the different velocity curves: $d_R v_{\rm rot}(0)$ derived from the observed Hα rotation curves, $d_R v_{\rm c}(0)$ computed from the circular velocity curves after ADC correction, and $d_R v_*(0)$ as derived from the stellar mass maps.

We see in the rotation curves (figures in Appendix C) that there are very few galaxies in which ADC is important. Moreover, ADC in the centre is negligible in most of the cases because either the dispersion in the centre is very low or the scalelength is very large compared to the radii, leading to $d_R v_{\rm rot}(0) \approx d_R v_{\rm c}(0)$. In Fig. 3, we compare $d_R v_{\rm rot}(0)$ and $d_R v_{\rm c}(0)$ and confirm that ADC has little impact on the determination of the inner slopes.

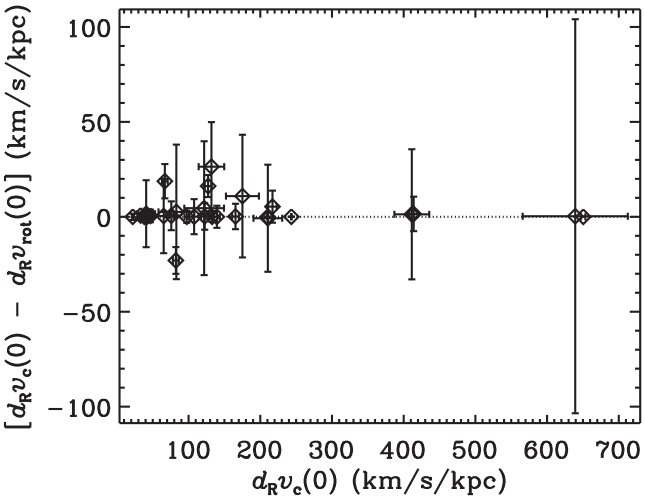

Figure 3. Comparison of the inner slopes derived from FP rotation curve with those derived from the circular velocity (after ADC). The differences are small except for NGC 1073, NGC 2500, NGC 2541 and NGC 6070.

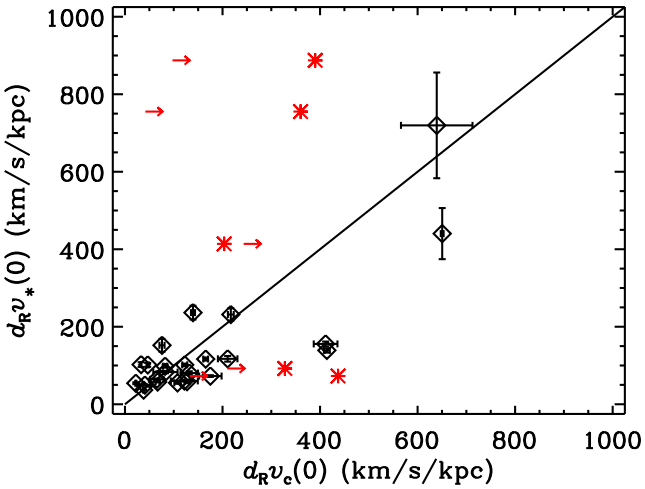

Figure 4. Comparison of the inner slopes derived from the ADC-based v_c with those from the stellar mass-derived rotation curves. The red arrows indicate values that are lower limits to the slopes, corresponding to galaxies with bad sampling in their central parts. We see that generally $d_R v_c(0) \geq d_R v_*(0)$ except for the lower limits. For those cases, we have computed the predicted value of the inner slope given by the scaling relation presented in LFV13, which we represent with red crosses.

The circular velocity of the galaxy is defined by the gravitational potential, which takes into account the total mass of the galaxy. Therefore, we expect all the components to influence the gravitational potential of the galaxy, and therefore the derived circular velocity:

$$v_c^2 = v_{gas}^2 + v_*^2 + v_{DM}^2. \quad (5)$$

Taking this into account, we expect to find that $v_c^2 > v_*^2$, and therefore $d_R v_c(0) > d_R v_*(0)$. In Fig. 4, we see that the cases where $d_R v_c(0) << d_R v_*(0)$ correspond to lower limits (marked with arrows) and $d_R v_c(0)$ is probably larger than $d_R v_*(0)$. Because these galaxies have an excess of light in their centres, the rotation curve derived from the stellar mass may have been overestimated when we assume a single stellar *M/L* throughout the galaxy (e.g. the starburst NGC 3504).

3.2 Relationships with central surface brightness and *T*-type

The aim of this study is to find possible relationships between the dynamics in the central parts of galaxies (by studying the inner slope of the rotation curve) and the formation, evolution and characteristics of those galaxies. First of all, we study the clearest known scaling relation between the inner slopes of the rotation curve and a feature of the galaxy, the one presented in LFV13. They find that $d_R V(0)$ correlates with the central surface brightness of the galaxies (μ_0), implying that regardless of the formation or evolution of the galaxy, the central stellar density closely relates to the inner shape of the potential well. The scaling relation for disc galaxies found by LFV13 is valid over more than two orders of magnitude in $d_R V(0)$ and four orders of magnitude in μ_0.

LFV13 measure μ_0 differentiating between disc-dominated galaxies (for which μ_0 is the linear extrapolation of the luminosity profile in the inner few arcseconds to $R = 0$) and bulge-dominated galaxies (for which μ_0 is estimated by adding the contributions of the disc to those of the bulge, measured by extrapolating from a Sérsic fit to the inner parts after the disc contribution has been removed). We measure μ_0 from the light profiles derived with ellipse fitting to the 3.6 μm images (Muñoz-Mateos et al. 2015), following the same procedures in LFV13. The galaxy inclinations have been obtained from Paper II.

We reproduce the relationship in LFV13, obtaining similar results. In Fig. 5, we see that $d_R v_c(0)$ and $d_R v_*(0)$ correlate with μ_0, with Pearson correlation coefficients of $|\rho| = 0.77$ and $|\rho| = 0.83$, respectively. As in the previous section, the points with the largest deviation from the inner slope predicted by LFV13 are the lower limits. As in LFV13, the scatter can come from observational uncertainties on the slopes, but can also be intrinsically linked to the determination of μ_0 with the 3.6 μm images (affected by star formation and the different structural components such as bars, bulges or nuclear activity). The correlation with $d_R v_*(0)$ is expected, as the stellar rotation curves have been derived directly from the 3.6 μm photometry.

To better make clear the interrelations between some galaxy properties and better understand the physical parameter that could be driving the rotation curve shape, we show in Fig. 6 the morphological *T*-type and μ_0 as a function of the mass of the bulge (M_{bulge}), a parameter that directly indicates the mass in the central parts. We compute the mass of the bulge (M_{bulge}) as $M_{bulge} = M_* \times B/T$, where M_* is the total stellar mass and B/T is the bulge-to-total ratio, assuming that the M/L does not change throughout the galaxy. B/T is obtained from multicomponent decompositions by Salo et al. (2015), where the 2D flux distribution is fitted with multiple Sérsic or Ferrers functions, representing the bulge, disc and bar. In some cases two disc components were fitted. In contrast to simple bulge/disc decompositions this approach ensures that the flux of the bar is not erroneously attributed to the bulge. μ_0 correlates with the morphological *T*-type (Fig. 6, top), although *T* is not a physical quantity. In Fig. 6, we show clear correlations between *T*-type and M_{bulge} (top left), as well as between μ_0 and M_{bulge} (bottom left).

Because there is a correlation between the morphological *T*-type and μ_0 ($\mu_0 \approx 0.65{*}T + 15.53$, Fig. 6), we derive that the LFV13 relation (equation 8 in LFV13) would predict a correlation between the morphological *T*-type and the inner slope of the rotation curve of $\log[d_R v_c(0)] \approx -0.14{*}T$. We find (from Fig. 6):

$$\log[d_R v_c(0)] = -0.14(\pm 0.01) * T + 2.72(\pm 0.04) \quad \text{and} \quad (6)$$

$$\log[d_R v_*(0)] = -0.12(\pm 0.02) * T + 2.59(\pm 0.09). \quad (7)$$

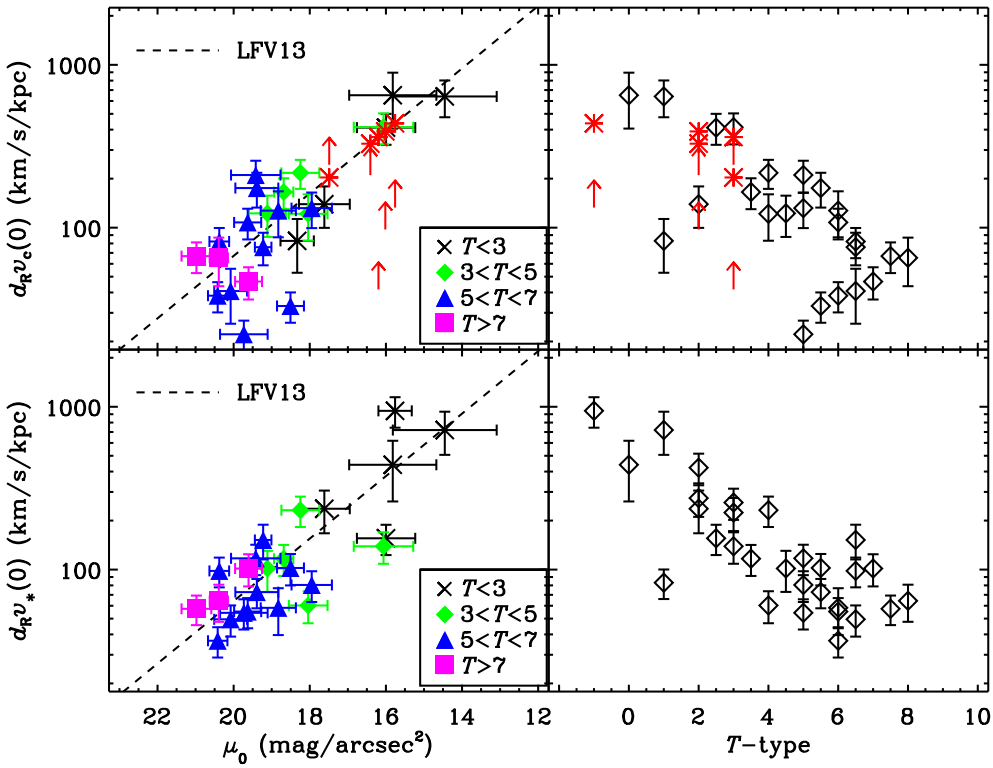

Figure 5. Inner slopes derived from the circular velocity curves ($d_R v_c(0)$, top) and from the stellar-derived curve ($d_R v_*(0)$, bottom) as a function of the central surface brightness (μ_0, left) and morphological T-type (right). The dashed line corresponds to the relationship found in LFV13. As in LFV13, we have divided our sample by morphological type: diamonds correspond to galaxies with T-type below 3, crosses correspond to galaxies with $3 < T < 5$, triangles correspond to galaxies with $5 < T < 7$ and squares correspond to galaxies with $T > 7$. We expect the correlations between the inner slopes and T-type, as the latter correlates with μ_0 (Fig. 6), and μ_0 correlates with the logarithm of $d_R v_c(0)$ (LFV13; Fig. 2). This correlation may be useful to obtain a measurement of $d_R v_c(0)$ and $d_R v_*(0)$ where one does not have information on the central surface brightness but about the morphological T-type. The red arrows correspond to lower limits of $d_R v_c(0)$ (for galaxies whose central parts were not fully sampled). The red crosses correspond to the predicted inner slope of those lower limits (based on their μ_0 and following equation 4 in LFV13).

The Pearson correlation coefficient between $\log[d_R v_c(0)]$ and T is $|\rho| = 0.74$, whereas that for $\log[d_R v_*(0)]$ and T is $|\rho| = 0.79$. This relationship can also be a proxy for the computation of the inner slope of the inner rotation curve. Of course, the morphological type is not a measured physical quantity and is defined for galaxies with and without discs, but this relationship can be useful when one does not have information about the surface brightness and wants to estimate the inner slope of the rotation curve.

3.3 Relationships with stellar mass and maximum rotational velocity

In the previous section, we have seen that the central surface brightness in the inner parts of galaxies correlates with the steepness of the inner rotation curve. We now want to know if there is also a relationship between the dynamics in the centres of galaxies and the gravitational potential of the whole galaxy. To do so, we compare the measured inner slopes with physical properties related with the *total* mass of a galaxy: total stellar mass M_* (which dominates the baryonic mass), and the maximum velocity. In Fig. 7, we represent $d_R v_c(0)$ and $d_R v_*(0)$ as a function of the total stellar mass ($\log M_*$) and the maximum circular velocity ($v_{c,max}$). Note that for NGC 2805, NGC 4324 and NGC 4389, $v_{c,max}$ is a lower limit as we do not see that the curve has reached a maximum or flat part.

We find no linear correlations, but we can identify some trends in the sense that steeper inner slopes correspond to the more massive galaxies, with higher $v_{c,max}$. Also, the total stellar mass and $v_{c,max}$ limit the inner slope, and low-mass galaxies (with lower $v_{c,max}$) only have slow-rising rotation curves. It is well known that for disc galaxies, the higher the stellar mass of a galaxy, the higher its maximum rotation velocity (Tully–Fisher relation, Tully & Fisher 1977). Here, we see that $d_R v_*(0)$ increases with $v_{*,max}$. However, these weak trends may arise from the relationship between the total stellar mass (and maximum circular velocity) with the mass of the bulge. We see in Fig. 8 that there is a good correspondence between M_{bulge} and M_* (or $v_{c,max}$).

3.4 Relationships with bar and bulge parameters

In the previous section, we have seen that the total stellar mass does not determine the inner slope of the rotation curve. Therefore, as the central surface brightness does correlate with the inner slope of the rotation curve (Section 3.2), we need to investigate further those structural components of galaxies that play a role in galaxy evolution and participate in the distribution of light, and thus mass, within the galaxy.

We explore here whether the structural parameters (such as the presence and properties of a bar or bulge) have an impact on the shape and inner slope of the rotation curve. If bars and bulges modify the mass distribution of a galaxy, the dynamics should be consistent with this new distribution. To study this, we represent in Figs 9–10 $d_R v_c(0)$ and $d_R v_*(0)$ as a function of bar strength (indicated by

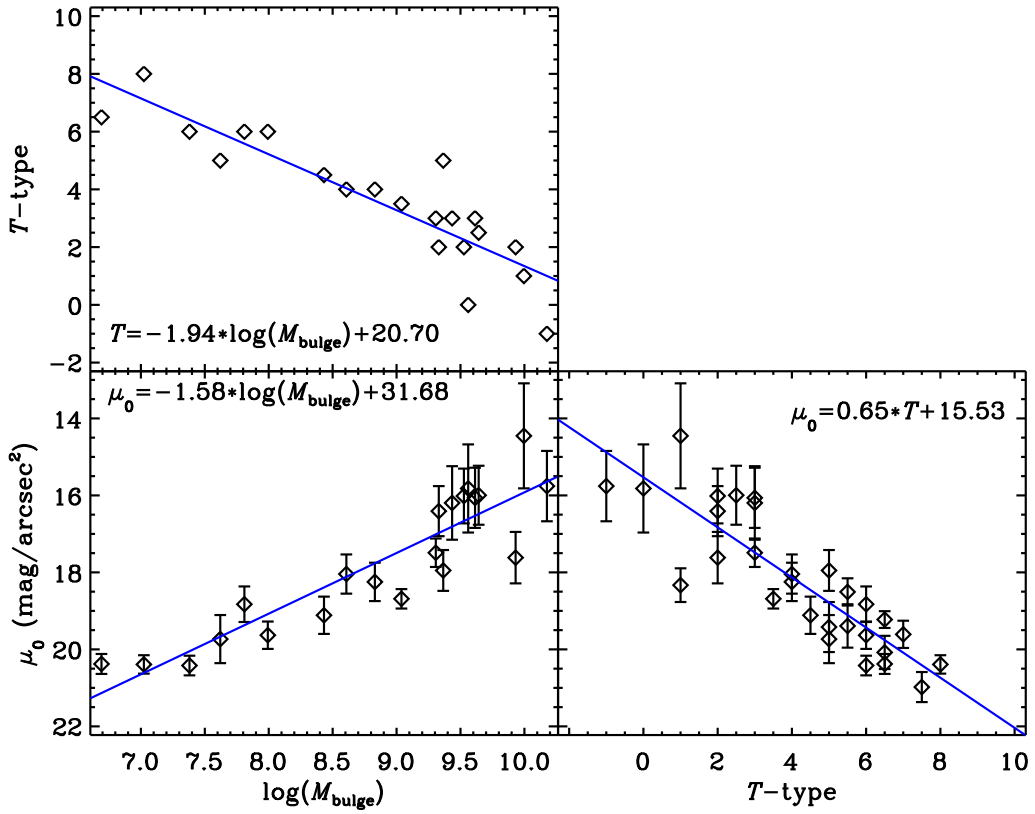

Figure 6. Left: correlations between the mass of the bulge ($M_{\rm bulge}$) and the morphological T-type (top) and μ_0 (bottom). Right: correlation between the morphological T-type and the central surface brightness. The blue straight lines are the linear fits to the data. We see that these parameters are correlated among them.

the $Q_{\rm b}$ and A_2 parameters), bar length and bulge-to-total light ratio (B/T). $Q_{\rm b}$ values have been measured from the torque maps derived from the 3.6 μm S^{4}G images (for a description of the method see Salo et al. 2010 and Laurikainen & Salo 2002), and are published in a compilation of bar strengths for the S^{4}G sample (Díaz-García et al. 2015). $Q_{\rm b}$ is strongly reacting to the bulge: a stronger bulge dilutes the tangential force from the bar and lowers $Q_{\rm b}$. Therefore, to distinguish the influence of the bulge in the bar strength, we represent galaxies with $B/T < 0.1$ with green squares, and galaxies with $B/T > 0.1$ with black diamonds. A_2 is the maximum of relative Fourier ($m = 2$) intensity amplitude I_2/I_0, and has been measured from the 3.6 μm images (Díaz-García et al. 2015). A_2 is a proxy of the strength of the bar, it measures how bright the bar is relative to the background. The radii of maximum torque in the radial force profiles have been chosen as a proxy for the bar length except when the torque maps do not present a clear butterfly pattern with an identifiable maximum at the bar region, in which case the bar lengths were measured visually (Herrera-Endoqui et al. 2015). The bar lengths have been normalized by the apparent major axis isophotal diameter (D_{25}), measured at or reduced to the surface brightness level $B = 25.0$ mag arcsec^{-2}, as explained in section 3.4.a, page 21, of Volume I of de Vaucouleurs et al. (1991). B/T ratios have been derived from the 2D decompositions of the 3.6 μm S^{4}G images. We refer the reader to Salo et al. (2015), where there is information about the method and the uncertainties in the derived parameters. It is important to note that, in some cases, the excess light in 3.6 μm due to star formation (SF) (e.g. NGC 3504) as well as the presence of a bar (if it has not been included in the decompositions, e.g. NGC 4151) can lead to an overestimation of B/T.

We find some limits, as in the relationships between inner slopes and mass: galaxies with high $Q_{\rm b}$ have slowly rising rotation curves, and steeper inner slopes tend to be found in galaxies with low $Q_{\rm b}$. Regarding A_2, the inner slopes are steeper for galaxies with higher A_2, and slowly rising rotation curves are found for galaxies with lower A_2. However, the weak trend between A_2 and the inner slope is largely driven by the extreme values of A_2. In Fig. 9, no clear correlation or trend is found when we only look at low B/T galaxies. Thus, for the cases where $Q_{\rm b}$ and A_2 measurements are not affected by a bulge, neither $Q_{\rm b}$ nor A_2 correlate with the rotation curve inner slope. These weak trends will be discussed in Section 4.

When we plot $d_R v_{\rm c}(0)$ and $d_R v_*(0)$ as a function of B/T (Fig. 10, top), we see a clear correlation between B/T and the inner slopes. Also, in the bottom panels of Fig. 10 we see that $d_R v_*(0)$ and $d_R v_{\rm c}(0)$ are correlated with the mass of the bulge, but not as much as B/T. In Section 4, we will discuss the physical consequences of this difference.?vsp -2pt?>

3.5 Relationships with star formation

Finally, we want to explore if the steepness of the rotation curve is influenced by the star formation. During star formation events, repeated supernova explosions in the core of the galaxies can result in not only an expulsion of gas from the central parts, but also to a re-distribution of DM (e.g. Pontzen & Governato 2012). Thus, as SFR is a proxy for the supernova rate (and therefore energy injection into the potential), we might expect changes in the dynamics of the central parts of galaxies (see e.g. LFV14). To check this, we measure the massive SFR as determined from the Hα images, the total SFR

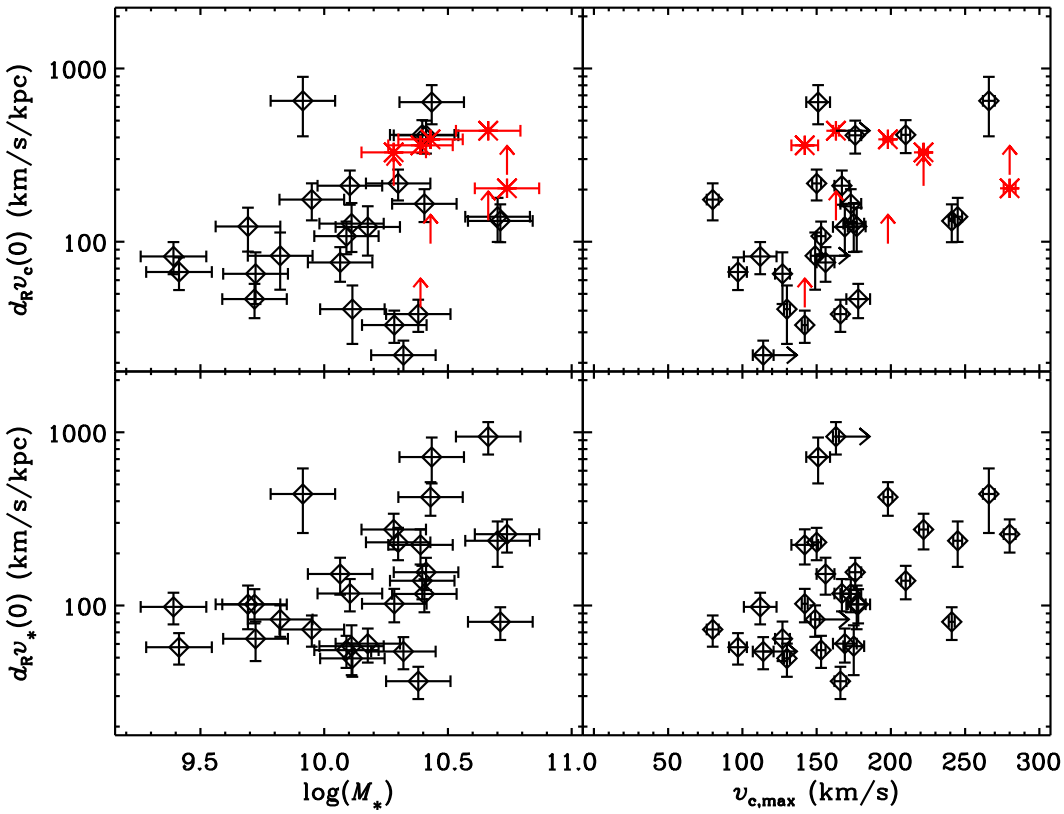

Figure 7. Rotation curve inner slopes $d_R v_c(0)$ and $d_R v_*(0)$ as a function of the total stellar mass (log M_*, left) and the maximum circular velocity ($v_{c,max}$, right). We find no correlations between the inner slopes and log M_*, but the total stellar mass limits the inner slope: steep slopes are found only in more massive galaxies, whereas lower mass galaxies present only low values of the inner slopes. As seen in the relationships with the total stellar mass, $v_{c,max}$ limits the inner slopes (steeper inner slopes are found for galaxies with higher $v_{c,max}$ and galaxies with low $v_{c,max}$ just have low-rising inner slopes). Note that for NGC 2805, NGC 4324 and NGC 4389, $v_{c,max}$ is a lower limit (marked with blue arrows that point to the right) as the curve has not reached a maximum or flat part, but continues to rise. The red arrows that point upwards correspond to lower limits of $d_R v_c(0)$ (for galaxies whose central parts were not fully sampled). The red crosses correspond to the predicted inner slope of those lower limits (based on their μ_0 and following equation 4 in LFV13).

(Hα). Furthermore, we measure the SFR densities (ΣSFRs) as the SFR normalized by the physical area (in kpc^2).

In Fig. 11, we represent $d_R v_c(0)$ and $d_R v_*(0)$ as a function of the total SFR and total ΣSFR. There is no correlation between these quantities and the inner slope of the inner part of the rotation curve, although this correlation was found in LFV14 for dwarf starbursts and irregular galaxies (see Fig. 11). This lack of correlation will be discussed in Section 4

3.6 Statistical significance of linear relationships

Our sample galaxies show a wide spread in characteristics: we have barred and unbarred galaxies, galaxies with and without bulges and galaxies hosting AGN. In the previous subsections, we have presented several plots that relate the results from the rotation curve analysis (the slope of the inner part of the ADC-corrected circular velocity curve $d_R v_c(0)$, and the slope of the inner part of the stellar mass derived velocity curve $d_R v_*(0)$) to a series of galaxy parameters. We have fitted linear functions to the data-points and computed the inner slopes as a function of these galaxy parameters. Here, we collect all the resulting fits with the correspondent correlation coefficient. When we write the equation of a line as $Y = a \times X + b$, Y is the dependent variable (log[$d_R v_c(0)$] and log[$d_R v_*(0)$]), X is the independent variable [μ_0, T-type, log(M_*), v_{max}, log(Q_b), log(A_2), log(r_{bar}/D_{25}), log(B/T), log(M_{bulge}), log(SFR$_{tot}$) and ΣSFR$_{tot}$] and a and b are the inner slope and y-intercept of the line fitted to the points. In Table 4, we present a and b for the linear fits to both $d_R v_c(0)$ and $d_R v_*(0)$. We also present the absolute value of the Pearson correlation coefficient ρ for each linear fit, where $|\rho| = 0$ means no correlation and $|\rho| = 1$ corresponds to a perfect linear correlation.

Inspection of Table 4 gives us hints about which parameters are important in determining the inner slope of the rotation curve. In the following section, we discuss the implications of the presence (or absence) of correlations as extracted from this table.

4 DISCUSSION

We want to explore whether we can identify changes in the distribution of mass to constrain the evolutionary processes that a galaxy has undergone. Here, we study the imprints of the internal secular evolution on the internal dynamics of a galaxy. Specifically, we consider the impact of the presence of a bar, the growth of a pseudo-bulge or star formation on the measurements of the inner slopes of the ADC-corrected circular velocity ($d_R v_c(0)$) and of the stellar mass derived rotation curve ($d_R v_*(0)$).

4.1 Bars

Bars are the most important drivers of secular evolution in galactic discs. They get stronger, longer and thinner over time (Athanassoula 2003; Gadotti 2011), and change the distribution of material in a

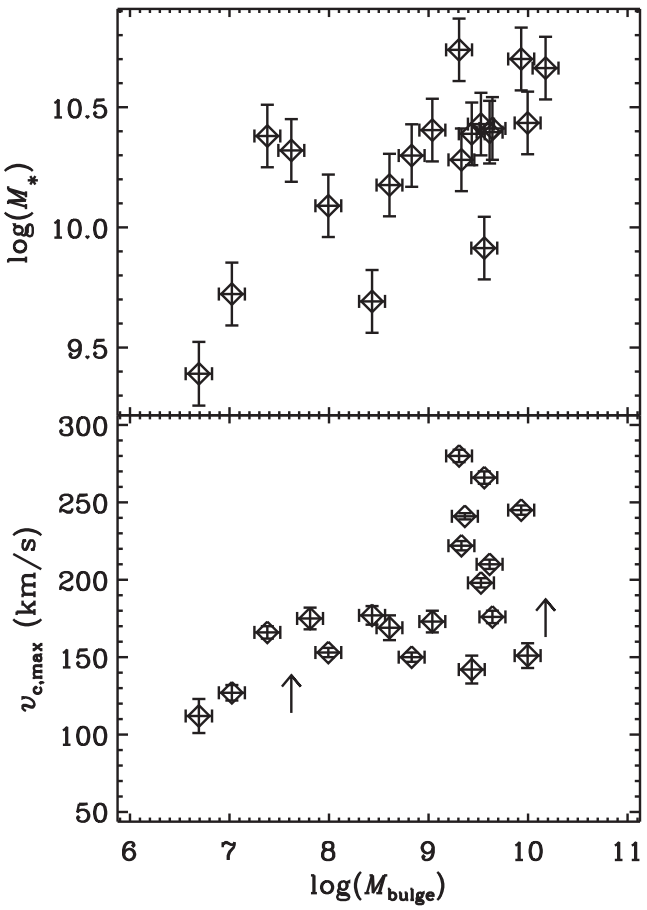

Figure 8. Relationship between the total stellar mass (top) and maximum circular velocity (bottom) as a function of the bulge mass. These parameters are well correlated, hence the weak trends between the inner slopes and $M_*/v_{c,max}$ (Fig. 7) may be driven by the tighter correlations between M_{bulge} and M_* (or $v_{c,max}$), as shown here.

galaxy, pushing the mass inside the corotation radius (CR) towards the centre, and the material outside the CR outwards.

We have in particular studied Q_b, a parameter which represents the bar strength. By definition, Q_b is influenced by the presence of the bulge, as Q_b decreases with increasing axisymmetric radial force. Therefore, Q_b anticorrelates with *B/T* by definition and it is known that Q_b increases towards later Hubble types (e.g.; Buta et al. 2005; Laurikainen et al. 2007).

In Fig. 9, we see that Q_b and the normalized length of the bar do not determine the inner slope of the rotation curve, although there is a moderate trend that the higher Q_b, the lower the inner slope. However, the presence of the bulge (as implicitly present in the parameter Q_b) can be seen: strong bulges dilute the tangential force. The possible anticorrelation between the inner slopes and Q_b may come from the bulge dilution effect (discussed for example in Laurikainen et al. 2004): Q_b is smaller for those galaxies which have steeper inner rotation curves, which means more mass concentration in the form of bulges, whereas Q_b is larger for galaxies which have smaller bulges or no bulges at all, but also shallower rotation curves in the central regions (for lack of a central mass concentration).

A similar scenario occurs when we use A_2, because A_2 increases with the presence of a bulge (B/T), and the inner slopes increase with A_2. We cannot prove that the strength of the bar does not influence the inner slope of the rotation curve, because the measurements we use depend on the presence of the bulge. We do find however that for low B/T galaxies, the bar strength as measured by Q_b or A_2 does not significantly correlate with the rotation curve inner slope, suggesting that bars are not a primary driver of the inner slope. Bars can, however, cause local deviations from the rotational motion, what we know as non-circular motions (see Paper II). A possible caveat in this study is that the inner slopes have been measured from the rotation curves, which average the velocities azimuthally. Therefore, the *local* deviations in the inner slope caused (azimuthally) by the bar may disappear in a rotation curve.

4.2 Bulges

Following Newton's law, we expect that the higher the concentration of material in the centres of galaxies, the steeper the inner slope. Corradi & Capaccioli (1990), Verheijen (1997), Sancisi (2004), Noordermeer et al. (2007) and Noordermeer (2008) agree that a greater concentration of material and light (specifically, in systems with bulges) is translated into a steeper inner slope. Analysing the possible influence of the bulge on the inner slope of the rotation curve, we see in Fig. 10 that the presence of the bulge indeed matters, as when *B/T* and M_{bulge} increase, $d_R v_c(0)$ and $d_R v_*(0)$ increase too, with a linear correlation with $|\rho| > 0.75$. Also, the correlation between M_{bulge} and $d_R v_*(0)$ indicates that the bulge mass plays a fundamental role in the stellar dynamics ($|\rho| = 0.78$).

Regarding the nature of the bulges, it is possible to classify them in three types: classical bulges, disky (pseudo-)bulges and boxy-peanut pseudo-bulges. Classical bulges are similar to elliptical galaxies (Davies et al. 1983; Franx 1993; Wyse, Gilmore & Franx 1997 and references therein), composed by old stellar populations and probably formed by hierarchical merging of smaller objects. Furthermore, the redistribution of material caused by the bar torque can result in central regions with higher density, often called disky pseudo-bulges or simply disky bulges, which are thought to be formed through internal, secular evolution (Athanassoula 1992, 2008; ; Wada & Habe 1992, 1995; Friedli & Benz 1993; Heller & Shlosman 1994; Knapen et al. 1995; Sakamoto et al. 1999; Sheth et al. 2003; Kormendy & Kennicutt 2004; Regan & Teuben 2004; Heller, Shlosman & Athanassoula 2007a,b; Fisher, Drory & Fabricius 2009; Kormendy 2013). Boxy-peanut bulges are the inner parts of bars seen edge-on, see Athanassoula (2005), and might be visible in face-on view as a barlens (Laurikainen et al. 2011, 2014; Athanassoula et al. 2015; Laurikainen & Salo 2016).

From the 2D decompositions of the 3.6 μm images (Salo et al. 2015), we have derived the brightness profiles of the bulges. These follow Sérsic (1968) function brightness profiles, which can be used as a proxy to determine if a bulge is a classical or a disky bulge (see details in, e.g. Kormendy & Kennicutt 2004; Fisher & Drory 2008; Gadotti 2009; Laurikainen & Salo 2016). Most disky bulges have Sérsic index $n < 2$ (although some disky bulges have been found to have $n \approx 4$), whereas many classical bulges have $n \gtrsim 2$. All the bulges in our sample have $n < 2$ except for those in NGC 691, NGC 4324 and NGC 4639. Another criterion of whether a bulge is classical or disky is *B/T*. Although small *B/T* values do not imply that a bulge is disky, large $B/T > 0.6$ correspond exclusively to classical bulges. All the *B/T* values of our galaxies are below 0.6, so this criterion cannot confirm anything. Buta et al. (2015) classify NGC 2543 and NGC 4639 as barlenses (therefore, boxy pseudo-bulges). More data would be necessary to confirm the nature of our bulges, but it is likely that none of our galaxies host a massive classical bulge. However, and regardless of the nature of the bulge, the greater concentration of material in the

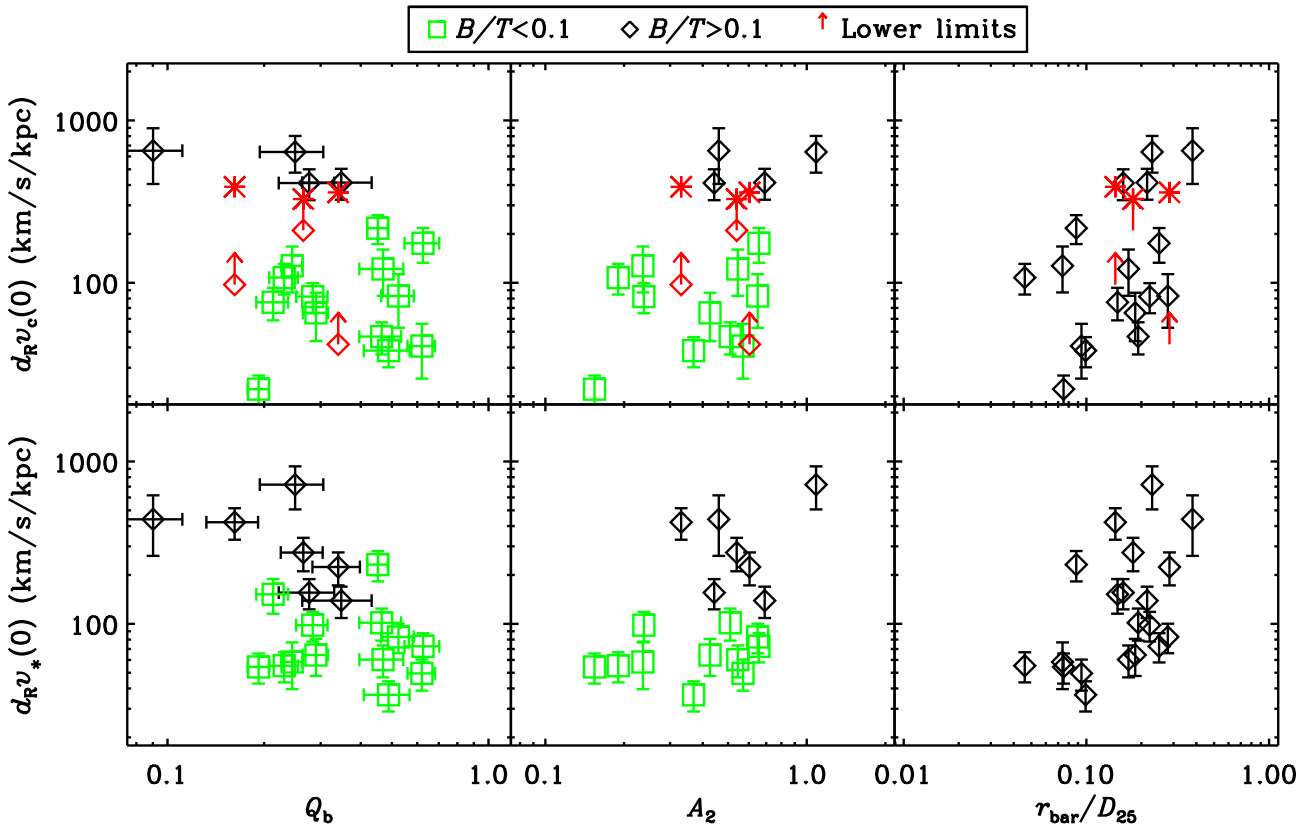

Figure 9. Rotation curve inner slopes $d_R v_c(0)$ and $d_R v_*(0)$ as a function of Q_b (left), A_2 (middle) and the bar length normalized by D_{25} (right). Due to the possible influence of the bulge on the determination of Q_b, we have differentiated between galaxies with $B/T < 0.1$ and $B/T > 0.1$. All the galaxies with lower limits have $B/T > 0.1$. We see that Q_b decreases with the slope and that the higher A_2, the steeper the slope. The red arrows correspond to lower limits of $d_R v_c(0)$ (for galaxies whose central parts were not fully sampled). The red crosses correspond to the predicted inner slope of those lower limits (based on their μ_0 and following equation 4 in LFV13).

bulge significantly influences the central dynamics of the galaxies in our sample. We see that the tendency of higher central light concentration and steeper inner slopes indicates that the luminous matter dominates the gravitational potential in the central parts of our galaxies. This statement is in agreement with previous studies, e.g. Lelli (2014).

4.3 Star formation

Another fundamental process taking place within galaxies is SF. To understand whether SF changes the rotation curve inner slopes and thus the central dynamics of the galaxy, we represented the total SFR and ΣSFRs as function of $d_R v_c(0)$ and $d_R v_*(0)$ (Fig. 11). We see that there is no correlation among these parameters, implying that SF does not determine the inner slope of the rotation curve in our sample galaxies. LFV14 find a correlation between ΣSFR and the circular velocity gradient for their sample of dwarf starbursts and irregulars. Thus, a possible explanation for the lack of correlation in this study is the difference in galaxy types with respect to those of LFV14. They study systems with one main structural component: a star-forming exponential disc, whereas our galaxies are formed by more than one structural component (i.e. bulges, spiral arms, bars). In a single-component system, the relation between internal dynamics (disc stability) and SF can be easily discerned, i.e. galaxies with steeper rotation curves have more stable gas discs, hence the gas densities can reach higher values, leading to higher SFRs. For multicomponent systems, however, the central non-star-forming components will also affect the value of the inner slope of the rotation curve, and therefore a simple relation between internal dynamics and the overall star formation may be more difficult to observe.

5 CONCLUSIONS

In this paper, we have studied the relationship between the kinematics in the innermost parts of galaxies and several key galaxy parameters. We study the innermost parts (few kpc) of the rotation curves of 29 spiral galaxies of all types with high angular (seeing limited, ∼1 arcsec) and spectral (∼8 km s^{-1} sampling) resolution FP data, and quantify the inner slope of the rotation curves with high precision. We compare the inner slopes obtained from the circular velocity curves (Hα rotation curves corrected for ADC), $d_R v_c(0)$, and those obtained from the velocity curves derived from stellar mass maps, $d_R v_*(0)$, with several galaxy parameters, and reach the following conclusions.

(i) The total stellar mass and the maximum rotational velocity limit the inner slope: steep slopes are only found in more massive galaxies (with higher $v_{c,max}$), and low-mass galaxies (galaxies with low $v_{c,max}$) only have shallow inner slopes. However, this trend may arise from the relationship between the total stellar mass and the mass of the bulge.

(ii) We confirm that the central surface brightness (μ_0) correlates with the inner slope of the rotation curve. We find another related

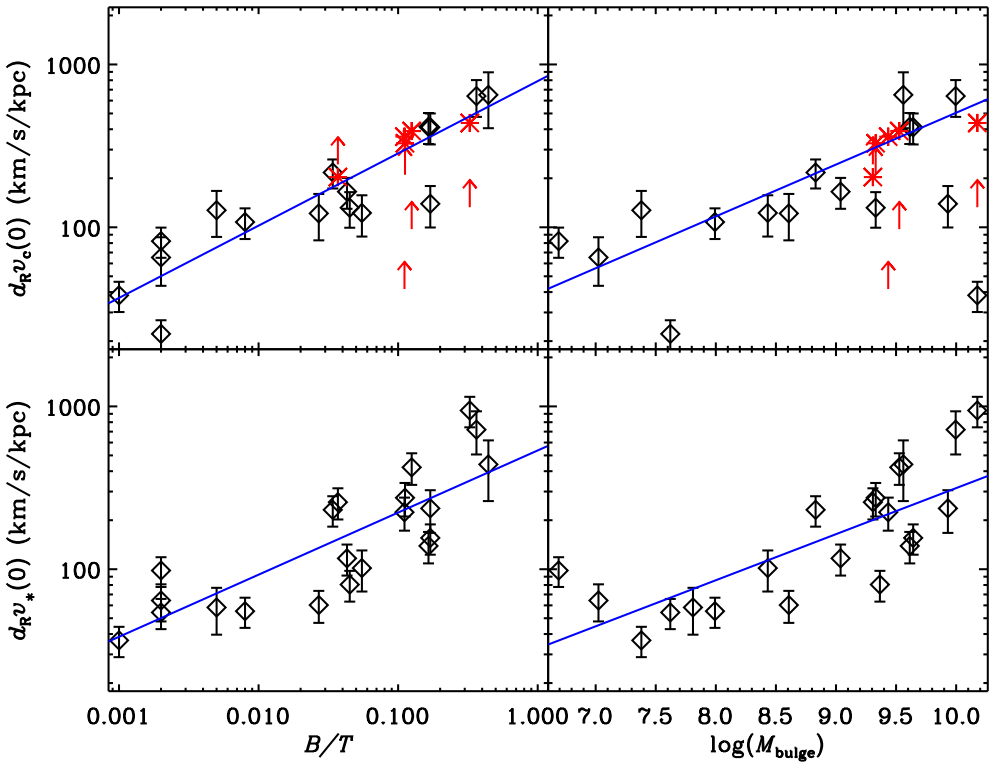

Figure 10. Rotation curve inner slopes $d_R v_c(0)$ and $d_R v_*(0)$ as a function of the bulge-to-total ratio B/T (left) and the bulge mass M_{bulge} (right). There is a moderate tendency that the more prominent the bulge, the steeper the inner slope. We see that the trends are clearer in the $d_R v_*(0)$ (bottom) plots. Note that only the galaxies with bulges have been considered. The red arrows correspond to lower limits of $d_R v_c(0)$ (for galaxies whose central parts were not fully sampled). The red crosses correspond to the predicted inner slope of those lower limits (based on their μ_0 and following equation 4 in LFV13).

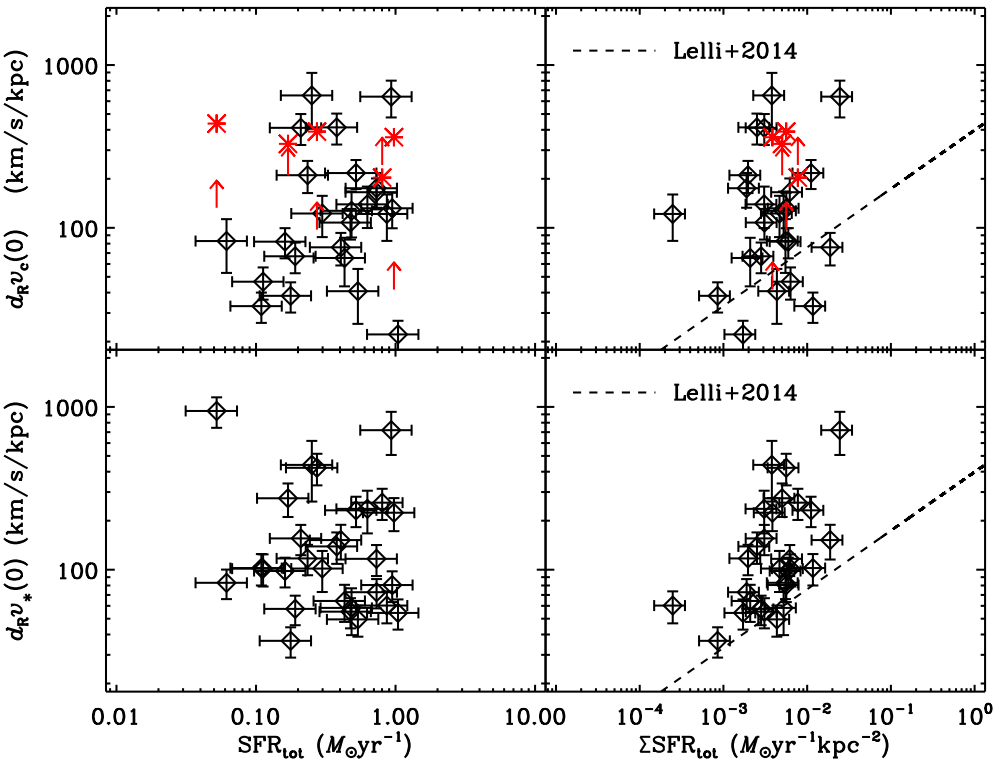

Figure 11. Rotation curve inner slopes $d_R v_c(0)$ and $d_R v_*(0)$ as a function of the total SFR (left) and ΣSFR$_{tot}$ (right). The red arrows correspond to lower limits of $d_R v_c(0)$ (for galaxies whose central parts were not fully sampled). The red crosses correspond to the predicted inner slope of those lower limits (based on their μ_0 and following equation 4 in LFV13). The dashed line in the right-hand panels shows the relation found for low-mass starburst and irregular galaxies by LFV14.

Table 4. Linear fits and their correlation coefficients. The equation of a line is $Y = a \times X + b$, where Y is the dependent variable ($\log[d_R v_c(0)]$ and $\log[d_R v_*(0)]$), X is the independent variable (the parameters) and a and b are the slope and y-intercept of the line fitted to the points. We present the absolute value of the Pearson correlation coefficient ρ for each linear fit, where $|\rho| = 0$ means no correlation and $|\rho| = 1$ corresponds to a perfect linear correlation. The table is ordered by the correlation coefficient $|\rho|$, being higher for the top four parameters (good correlation) and lower for the other parameters (not that good or lack of correlation).

	$\log[d_R v_c(0)] = a \times$ parameter $+ b$			$\log[d_R v_*(0)] = a \times$ parameter $+ b$		
	a	b	$\lvert\rho\rvert$	a	b	$\lvert\rho\rvert$
$\log(B/T)$	0.44 ± 0.03	2.90 ± 0.05	0.90	0.38 ± 0.03	2.73 ± 0.05	0.82
μ_0	−0.24 ± 0.02	6.49 ± 0.41	0.84	−0.20 ± 0.02	5.82 ± 0.36	0.83
$\log(M_{\rm bulge})$	0.32 ± 0.02	−0.48 ± 0.16	0.81	0.28 ± 0.02	−0.33 ± 0.19	0.78
T-type	−0.14 ± 0.01	2.72 ± 0.04	0.74	−0.12 ± 0.02	2.59 ± 0.09	0.79
$\log(A_2)$	1.16 ± 0.11	2.62 ± 0.05	0.48	0.58 ± 0.11	2.23 ± 0.05	0.44
$\log(r_{\rm bar}/D_{25})$	0.86 ± 0.10	2.87 ± 0.09	0.47	0.58 ± 0.10	2.52 ± 0.08	0.49
$v_{\rm c.max}$	0.004 ± 0.001	1.45 ± 0.08	0.44	0.003 ± 0.001	1.53 ± 0.07	0.43
$\log(Q_{\rm b})$	−3.29 ± 9.45	0.58 ± 4.87	0.38	−2.44 ± 6.91	0.87 ± 3.57	0.51
$\log(M_*)$	0.43 ± 0.05	−2.27 ± 0.54	0.36	0.43 ± 0.05	−2.27 ± 0.52	0.42
$\log(\Sigma{\rm SFR})$	0.20 ± 0.05	2.60 ± 0.13	0.18	0.42 ± 0.05	3.06 ± 0.12	0.53
$\log({\rm SFR})$	10.03 ± 10.15	6.81 ± 4.72	0.07	−5.48 ± 3.37	−0.44 ± 1.63	0.12

scaling relation for disc galaxies: a relationship between the morphological T-type and $d_R v(0)$. This implies that for early-type to late-type spirals, the morphological type of a galaxy is related to the dynamics in the central parts of galaxies, quite plausibly through the radial mass distribution.

(iii) Although a bar can be expected to affect the distribution of material in the central parts of their host galaxies, a singular measurement of the bar strength which is unaffected by the presence of the bulge remains elusive, and therefore limit any conclusion on how bars influence the rotation curve inner slope. We do find, however, that for low B/T galaxies, the bar strength as measured by $Q_{\rm b}$ or A_2 does not significantly correlate with the rotation curve inner slope, suggesting that bars are not a primary driver of the inner slope.

(iv) The fact that higher B/T and $M_{\rm bulge}$ are correlated with the inner slope indicates that bulges play a role in the dynamics of the central parts of galaxies. A higher concentration of stellar mass in the centres of galaxies is translated into steeper inner slopes, confirming that baryonic mass dominates the dynamics in the inner regions.

ACKNOWLEDGEMENTS

We thank Mauricio Cisternas and Dimitri Gadotti for useful comments during the preparation of this manuscript. The authors thank the entire S^{4}G team for their efforts in this project. We thank the referee for his comments, which improved the quality of the paper. We acknowledge financial support to the DAGAL network from the People Programme (Marie Curie Actions) of the European Union's Seventh Framework Programme FP7/2007-2013/ under REA grant agreement number PITN-GA-2011-289313, and from the Spanish MINECO under grant numbers AYA2007-67625-CO2-O2 and AYA2013-41243-P. This work was co-funded under the Marie Curie Actions of the European Commission (FP7-COFUND). We also gratefully acknowledge support from NASA JPL/Spitzer grant RSA 1374189 provided for the S^{4}G project. JHK thanks the Astrophysics Research Institute of Liverpool John Moores University for their hospitality, and the Spanish Ministry of Education, Culture and Sports for financial support of his visit there, through grant number PR2015-00512. EA and AB thank the CNES for support. JCMM acknowledges support from the National Radio Astronomy Observatory, which is a facility of the National Science Foundation operated under cooperative agreement by Associated Universities, Inc. HS, EL and SC acknowledge the Academy of Finland for support. This research is based on observations made with the WHT operated on the island of La Palma by the Isaac Newton Group of Telescopes, in the Spanish Observatorio del Roque de Los Muchachos of the Instituto de Astrofísica de Canarias. We acknowledge the usage of the HyperLeda data base (http://leda.univ-lyon1.fr). This research has made use of the NASA/IPAC Extragalactic Database (NED) which is operated by JPL, Caltech, under contract with NASA.

REFERENCES

Athanassoula E., 1992, MNRAS, 259, 345
Athanassoula E., 2003, MNRAS, 341, 1179
Athanassoula E., 2005, MNRAS, 358, 1477
Athanassoula E., 2008, in Bureau M., Athanassoula E., Barbuy B., eds, Proc. IAU Symp. 245, Formation and Evolution of Galaxy Bulges. Cambridge Univ. Press, Cambridge, p. 93
Athanassoula E., Laurikainen E., Salo H., Bosma A., 2015, MNRAS, 454, 3843
Begeman K. G., 1987, PhD thesis, Univ. Groningen
Begeman K. G., 1989, A&A, 223, 47
Binney J., Tremaine S., 2008, Galactic Dynamics, 2nd edn. Princeton Univ. Press, Princeton, NJ
Blais-Ouellette S., Amram P., Carignan C., Swaters R., 2004, A&A, 420, 147
Bosma A., 1978, PhD Thesis, Univ. Groningen
Bosma A., 1981, AJ, 86, 1791
Bosma A., Ekers R. D., Lequeux J., 1977, A&A, 57, 97
Broeils A. H., 1992, PhD thesis, Univ. Groningen
Burstein D., Rubin V. C., 1985, ApJ, 297, 423
Buta R., Block D. L., 2001, ApJ, 550, 243
Buta R., Vasylyev S., Salo H., Laurikainen E., 2005, AJ, 130, 506
Buta R. J. et al., 2015, ApJS, 217, 32
Casertano S., 1983, MNRAS, 203, 735
Casertano S., van Gorkom J. H., 1991, AJ, 101, 1231
Chemin L. et al., 2006, MNRAS, 366, 812
Ciotti L., 1991, A&A, 249, 99
Ciotti L., Bertin G., 1999, A&A, 352, 447
Corradi R. L. M., Capaccioli M., 1990, A&A, 237, 36
Corradi R. L. M., Boulesteix J., Bosma A., Amram P., Capaccioli M., 1991, A&A, 244, 27
Côté S., Carignan C., Freeman K. C., 2000, AJ, 120, 3027

Davies R. L., Efstathiou G., Fall S. M., Illingworth G., Schechter P. L., 1983, ApJ, 266, 41
de Blok W. J. G., McGaugh S. S., van der Hulst J. M., 1996, MNRAS, 283, 18
de Grijs R., Peletier R. F., 1997, A&A, 320, L21
de Vaucouleurs G., de Vaucouleurs A., Corwin H. G., Jr, Buta R. J., Paturel G., Fouque P., 1991, Third Reference Catalogue of Bright Galaxies. Springer-Verlag, Berlin
Díaz-García S., Salo H., Laurikainen E., Herrera-Endoqui M., 2015, preprint (arXiv:1509.06743)
Epinat B., Amram P., Marcelin M., 2008, MNRAS, 390, 466
Erroz-Ferrer S. et al., 2012, MNRAS, 427, 2938 (Paper I)
Erroz-Ferrer S. et al., 2015, MNRAS, 451, 1004 (Paper II)
Fisher D. B., Drory N., 2008, AJ, 136, 773
Fisher D. B., Drory N., Fabricius M. H., 2009, ApJ, 697, 630
Franx M., 1993, in Dejonghe H., Habing H. J., eds, Proc. IAU Symp. 153, Galactic Bulges. Kluwer, Dordrecht, p. 243
Fricke K. J., Reinhardt M., 1974, A&A, 37, 349
Friedli D., Benz W., 1993, A&A, 268, 65
Gadotti D. A., 2009, MNRAS, 393, 1531
Gadotti D. A., 2011, MNRAS, 415, 3308
Gentile G., Salucci P., Klein U., Vergani D., Kalberla P., 2004, MNRAS, 351, 903
Heller C. H., Shlosman I., 1994, ApJ, 424, 84
Heller C. H., Shlosman I., Athanassoula E., 2007a, ApJ, 657, L65
Heller C. H., Shlosman I., Athanassoula E., 2007b, ApJ, 671, 226
Herrera-Endoqui M., Díaz-García S., Laurikainen E., Salo H., 2015, A&A, 582, A86
Ho L. C., Filippenko A. V., Sargent W. L. W., 1997, ApJ, 487, 591
Knapen J. H., Beckman J. E., Heller C. H., Shlosman I., de Jong R. S., 1995, ApJ, 454, 623
Kormendy J., 2013, in Falcón-Barroso J., Knapen J. H., eds, Secular Evolution of Galaxies. Cambridge Univ. Press, Cambridge, p. 1
Kormendy J., Kennicutt R. C., Jr, 2004, ARA&A, 42, 603
Laurikainen E., Salo H., 2002, MNRAS, 337, 1118
Laurikainen E., Salo H., 2016, in Laurikainen E., Peletier R., Gadotti D., eds, Astrophysics and Space Science Library, Vol. 418, Galactic Bulges. Springer-Verlag, Berlin, p. 77
Laurikainen E., Salo H., Buta R., Vasylyev S., 2004, MNRAS, 355, 1251
Laurikainen E., Salo H., Buta R., Knapen J. H., 2007, MNRAS, 381, 401
Laurikainen E., Salo H., Buta R., Knapen J. H., 2011, MNRAS, 418, 1452
Laurikainen E., Salo H., Athanassoula E., Bosma A., Herrera-Endoqui M., 2014, MNRAS, 444, L80
Lelli F., 2014, Galaxies, 2, 292
Lelli F., Fraternali F., Sancisi R., 2010, A&A, 516, A11
Lelli F., Verheijen M., Fraternali F., Sancisi R., 2012a, A&A, 537, A72
Lelli F., Verheijen M., Fraternali F., Sancisi R., 2012b, A&A, 544, A145
Lelli F., Fraternali F., Verheijen M., 2013, MNRAS, 433, L30 (LFV13)
Lelli F., Fraternali F., Verheijen M., 2014a, A&A, 563, A27 (LFV14)
Lelli F., Verheijen M., Fraternali F., 2014b, A&A, 566, A71
Matthews L. D., Gallagher J. S., III, 2002, ApJS, 141, 429
Meidt S. E. et al., 2012, ApJ, 744, 17
Meidt S. E. et al., 2014, ApJ, 788, 144
Muñoz-Mateos J. C. et al., 2009, ApJ, 703, 1569
Muñoz-Mateos J. C. et al., 2015, ApJS, 219, 3
Noordermeer E., 2008, MNRAS, 385, 1359
Noordermeer E., van der Hulst J. M., Sancisi R., Swaters R. A., van Albada T. S., 2005, A&A, 442, 137
Noordermeer E., van der Hulst J. M., Sancisi R., Swaters R. S., van Albada T. S., 2007, MNRAS, 376, 1513
Norris M. A., Meidt S., Van de Ven G., Schinnerer E., Groves B., Querejeta M., 2014, ApJ, 797, 55
O'dell C. R., Townsley L. K., 1988, A&A, 198, 283
Persic M., Salucci P., 1991, ApJ, 368, 60
Persic M., Salucci P., Stel F., 1996, MNRAS, 281, 27
Pontzen A., Governato F., 2012, MNRAS, 421, 3464
Querejeta M. et al., 2015, ApJS, 219, 5
Quillen A. C., Frogel J. A., Gonzalez R. A., 1994, ApJ, 437, 162
Regan M. W., Teuben P. J., 2004, ApJ, 600, 595
Relaño M., Beckman J. E., Zurita A., Rozas M., Giammanco C., 2005, A&A, 431, 235
Roberts M. S., Whitehurst R. N., 1975, ApJ, 201, 327
Röck B., Vazdekis A., Peletier R. F., Knapen J. H., Falcón-Barroso J., 2015, MNRAS, 449, 2853
Rogstad D. H., Shostak G. S., 1972, ApJ, 176, 315
Rubin V. C., Burstein D., Ford W. K., Jr, Thonnard N., 1985, ApJ, 289, 81
Sakamoto K., Okumura S. K., Ishizuki S., Scoville N. Z., 1999, ApJ, 525, 691
Salo H., Rautiainen P., Buta R., Purcell G. B., Cobb M. L., Crocker D. A., Laurikainen E., 1999, AJ, 117, 792
Salo H., Laurikainen E., Buta R., Knapen J. H., 2010, ApJ, 715, L56
Salo H. et al., 2015, ApJS, 219, 4
Sancisi R., 2004, in Ryder S., Pisano D., Walker M., Freeman K., eds, Proc. IAU Symp. 220, Dark Matter in Galaxies. Freeman, San Francisco, p. 233
Sancisi R., Allen R. J., Sullivan W. T., III, 1979, A&A, 78, 217
Sérsic J. L., 1963, Bol. Asociacion Argentina Astron. Plata Argentina, 6, 41
Sheth K., Regan M. W., Scoville N. Z., Strubbe L. E., 2003, ApJ, 592, L13
Sheth K. et al., 2010, PASP, 122, 1397
Sofue Y., 1996, ApJ, 458, 120
Sofue Y., 1997, PASJ, 49, 17
Speltincx T., Laurikainen E., Salo H., 2008, MNRAS, 383, 317
Swaters R. A., 1999, PhD thesis, Univ. Groningen
Swaters R. A., Madore B. F., van den Bosch F. C., Balcells M., 2003, ApJ, 583, 732
Swaters R. A., Sancisi R., van Albada T. S., van der Hulst J. M., 2009, A&A, 493, 871
Swaters R. A., Sancisi R., van Albada T. S., van der Hulst J. M., 2011, ApJ, 729, 118
Swaters R. A., Sancisi R., van der Hulst J. M., van Albada T. S., 2012, MNRAS, 425, 2299
Tully R. B., Fisher J. R., 1977, A&A, 54, 661
van Albada G. D., 1985, A&A, 142, 491
van Albada T. S., Sancisi R., 1986, Phil. Trans. R. Soc., 320, 447
van der Kruit P. C., Bosma A., 1978, A&AS, 34, 259
Verheijen M. A. W., 1997, PhD thesis, Univ. Groningen
Verheijen M. A. W., 2001, ApJ, 563, 694
Verheijen M. A. W., Sancisi R., 2001, A&A, 370, 765
Wada K., Habe A., 1992, MNRAS, 258, 82
Wada K., Habe A., 1995, MNRAS, 277, 433
Walter F., Brinks E., de Blok W. J. G., Bigiel F., Kennicutt R. C., Jr, Thornley M. D., Leroy A., 2008, AJ, 136, 2563
Westfall K. B., Bershady M. A., Verheijen M. A. W., Andersen D. R., Martinsson T. P. K., Swaters R. A., Schechtman-Rook A., 2011, ApJ, 742, 18
Wyse R. F. G., Gilmore G., Franx M., 1997, ARA&A, 35, 637

SUPPORTING INFORMATION

Additional Supporting Information may be found in the online version of this article:

Appendix A. Hα surface brightness profiles.
Appendix B. Velocity dispersion profiles.
Appendix C. Rotation curves (http://www.mnras.oxfordjournals.org/lookup/suppl/doi:10.1093/mnras/stw300/-/DC1).

Please note: Oxford University Press is not responsible for the content or functionality of any supporting materials supplied by the authors. Any queries (other than missing material) should be directed to the corresponding author for the article.

This paper has been typeset from a TEX/LATEX file prepared by the author.